

# Supplementary Information: Computer simulations show that liquid-liquid phase separation enhances self-assembly

Layne B. Frechette,\* Naren Sundararajan,\* Fernando Caballero, Anthony Trubiano, and Michael F. Hagan<sup>†</sup>  
*Martin Fisher School of Physics, Brandeis University, Waltham, Massachusetts 02453, USA*  
 (Dated: May 27, 2025)

## CONTENTS

S1. Model description	1
A. Dodecahedral capsid model	1
B. Icosahedral capsid model	2
C. Dynamics	3
S2. Partition coefficient calculation	3
A. Ideal solution theory	3
B. Hard sphere theory	3
S3. Equilibrium assembly theory	4
A. Ideal solution theory	4
B. Hard sphere theory	5
S4. Estimating parameters for the theoretical model	6
A. Estimating $\sigma_{\text{cap}}$	6
B. Estimating $f_{\text{capsid}}$	7
S5. Yield vs $\epsilon_{\text{ss}}$ at different times	7
S6. Scaling theory for assembly kinetics	7
S7. Additional supplementary figures	10
S8. Movie descriptions	14
References	14

## S1. MODEL DESCRIPTION

### A. Dodecahedral capsid model

In the dodecahedron model, each subunit consists of seven pseudoatoms of three different types. Five attractor pseudoatoms (‘A’), which facilitate subunit-subunit binding, are located at the vertices of a regular pentagon with circumradius  $l_0$ , which we take as the unit of length for this model. ‘A’ pseudoatoms on different subunits interact via a Morse potential:

$$u_{\text{AA}}(r) = \begin{cases} \epsilon_{\text{ss}} [e^{-2\alpha(r-r_0)} - 2e^{-\alpha(r-r_0)}] - \epsilon_0, & r \leq 2l_0 \\ 0, & r > 2l_0 \end{cases} \quad (\text{S1})$$

where  $r$  is the distance between ‘A’ pseudoatoms,  $r_0 = l_0/5$  is the distance at which the potential energy is minimized,  $\alpha = 2.5/r_0$  sets the width of the potential well, and  $\epsilon_0 = \epsilon_{\text{ss}} [e^{-2\alpha(2l_0-r_0)} - 2e^{-\alpha(2l_0-r_0)}]$  is chosen so that the potential

\* These two authors contributed equally.

<sup>†</sup> hagan@brandeis.edu

goes to zero continuously at  $r = 2l_0$ . The parameter  $\epsilon_{ss}$  sets the depth of the potential well and hence controls the subunit-subunit binding affinity. Additionally, each subunit contains one top pseudoatom ('T') and one bottom pseudoatom ('B') located at  $z = \pm l_0/2$  relative to the centroid of the pentagon, which lies in the  $xy$  plane in the body-fixed frame. 'T' pseudoatoms interact via a purely repulsive potential:

$$u_{TT}(r) = \mathcal{L}(r; \sigma_{TT}, \epsilon_{TT}), \quad (S2)$$

where:

$$\mathcal{L}(r; \sigma, \epsilon) = \begin{cases} 4\epsilon \left[ \left(\frac{\sigma}{r}\right)^{12} - \left(\frac{\sigma}{r}\right)^6 \right], & r \leq \sigma \\ 0, & r > \sigma. \end{cases} \quad (S3)$$

We choose  $\epsilon_{TT} = 1$  and  $\sigma_{TT} = 2.1l_0$ , which encourages a subunit-subunit binding angle consistent with a dodecahedron. 'B' pseudoatoms interact with 'T' pseudoatoms via a similarly repulsive potential:

$$u_{TB}(r) = \mathcal{L}(r; \sigma_{TB}, \epsilon_{TB}), \quad (S4)$$

where  $\epsilon_{TB} = \epsilon_{TT}$  and  $\sigma_{TB} = 1.8l_0$ . The 'T'-'B' interactions help prevent "upside down" assembly, by discouraging subunit-subunit binding that results in 'T' and 'B' pseudoatoms on different subunits being adjacent. Subunits and their interactions are depicted in Fig. 2A,B, and a dodecahedral capsid resulting from the assembly of twelve subunits is shown in Fig. 2C. SI Section S4B provides an estimate of the subunit-subunit binding affinity and capsid free energy as a function of  $\epsilon_{ss}$ .

## B. Icosahedral capsid model

The icosahedron model was previously developed to study the assembly of DNA origami capsids [1, 2]. The subunit shape and the interactions between the constituent pseudoatoms are designed such that the minimum energy configuration of a collection of twenty subunits is an icosahedral shell (see Fig. 2F). Subunits consist of 45 purely repulsive excluder pseudoatoms and six attractor pseudoatoms. As in the dodecahedron model, subunit-subunit binding affinities are governed by the parameter  $\epsilon_{ss}$ . However, unlike the dodecahedron model, not all attractor atoms interact with each other equally. Instead, each attractor pseudoatom within a subunit has a distinct type (represented as different colors in Fig. 2D,E). Pairs of complementary attractor atoms attract each other, while non-complementary attractor atoms interact only via excluded volume. This prevents subunits from binding "upside down" (thus it has a similar role to the repulsive 'T'-'B' interactions in the dodecahedron model). Complementary attractor pairs are listed in Table S1.

TABLE S1. Complementary attractors (1=complementary, 0=non-complementary)

	blue	red	gray	orange	yellow	tan
blue	0	1	0	1	0	1
red	1	0	1	0	1	0
gray	0	1	0	1	0	1
orange	1	0	1	0	1	0
yellow	0	1	0	1	0	1
tan	1	0	1	0	1	0

Excluder pseudoatoms and non-complementary attractor pseudoatoms interact via a Weeks-Chandler-Anderson (WCA) potential [3]:

$$u_{WCA}(r) = \begin{cases} 4\epsilon_{ss} \left[ \left(\frac{\sigma}{r}\right)^{12} - \left(\frac{\sigma}{r}\right)^6 + \frac{1}{4} \right], & r < 2^{1/6}\sigma \\ 0, & r \geq 2^{1/6}\sigma \end{cases} \quad (S5)$$

where  $r$  is the distance between pseudoatoms and  $\sigma$  is the pseudoatom diameter, which we take as the unit of length for this model. Complementary attractor pseudoatoms interact via a Lennard-Jones potential:

$$u_{ss}(r) = \begin{cases} u_{LJ}(r) - u_{LJ}(r_{cut}), & r < r_{cut} \\ 0, & r \geq r_{cut} \end{cases} \quad (S6)$$

where  $u_{\text{LJ}}$  is given by

$$u_{\text{LJ}}(r) = 4\epsilon_{\text{ss}} \left[ \left( \frac{\sigma}{r} \right)^{12} - \left( \frac{\sigma}{r} \right)^6 \right]. \quad (\text{S7})$$

and  $r_{\text{cut}} = 3\sigma$ . Two interacting subunits are depicted in Fig. 2E.

### C. Dynamics

Subunits (labeled  $i = 1, \dots, N$ ) evolve in time via Langevin dynamics:

$$m \frac{d\mathbf{v}_i}{dt} = \mathbf{F}_{\text{C},i} - \gamma \mathbf{v}_i + \mathbf{F}_{\text{R},i}, \quad (\text{S8a})$$

$$\mathbf{v}_i = \frac{d\mathbf{r}_i}{dt}, \quad (\text{S8b})$$

$$\mathbf{I} \frac{d\boldsymbol{\omega}_i}{dt} = \boldsymbol{\tau}_{\text{C},i} - \gamma_{\text{r}} \boldsymbol{\omega}_i + \boldsymbol{\tau}_{\text{R},i} \quad (\text{S8c})$$

$$\boldsymbol{\omega}_i = \frac{d\mathbf{q}_i}{dt}. \quad (\text{S8d})$$

Here  $m$  is the mass and  $\mathbf{I}$  is the inertia tensor of a subunit;  $\gamma$  and  $\gamma_{\text{r}}$  are translational and rotational friction constants;  $\mathbf{r}_i$  and  $\mathbf{v}_i$  are the center of mass position and velocity;  $\mathbf{q}_i$  and  $\boldsymbol{\omega}_i$  are the orientation and angular velocity;  $\mathbf{F}_{\text{C},i}$  and  $\boldsymbol{\tau}_{\text{C},i}$  are the conservative force and torque that come from the potential energy  $U$ , which includes a sum of pairwise interactions between pseudoatoms (Eqs. S1, S2, and S4 for the dodecahedron model; Eqs. S5 and S6 for the icosahedron model), a sum over single-pseudoatom energies due to the condensate potential (Eq. ??), and constraint forces that ensure rigid body motion. The quantities  $\mathbf{F}_{\text{R},i}$  and  $\boldsymbol{\tau}_{\text{R},i}$  are the random (thermal) force and torque, which have zero mean and variances given by:

$$\langle \mathbf{F}_{\text{R},i}(t) \cdot \mathbf{F}_{\text{R},j}(t') \rangle = 6k_{\text{B}}T\gamma\delta(t-t')\delta_{ij} \quad (\text{S9a})$$

$$\langle \boldsymbol{\tau}_{\text{R},i}(t) \cdot \boldsymbol{\tau}_{\text{R},j}(t') \rangle = 6k_{\text{B}}T\gamma_{\text{r}}\delta(t-t')\delta_{ij}. \quad (\text{S9b})$$

We set  $\gamma = 10$  and  $\gamma_{\text{r}} = 4\gamma/3$ , which makes the dynamics effectively overdamped (consistent with the viscous interior of a cell). Within HOOMD-blue [4], we use the velocity Verlet algorithm to solve Eqs. S8a, S8b, and the similarly symplectic integrator of Kamberaj et al. [5] to solve Eqs. S8c, S8d. We employ a timestep  $\Delta t = 5 \times 10^{-3}$ .

## S2. PARTITION COEFFICIENT CALCULATION

### A. Ideal solution theory

For sufficiently low concentrations of subunits within the condensate, ideal solution theory gives  $K_{\text{c}}^{\text{IS}} = \frac{\rho_{\text{c}}^{\text{c}}}{\rho_{\text{c}}^{\text{bg}}} = e^{\beta\epsilon_{\text{c}}}$ . For subunit densities and partition coefficients that lead to low packing fractions  $\eta$  within the condensate  $\eta \lesssim 10\%$  this theory predicts the measured partition coefficient with reasonable accuracy (Fig. 10 in main text). For larger values, we observe significant deviations between ideal solution theory and simulation results without assembly, in which we set  $\epsilon_{\text{ss}} = 0$  for attractor pseudoatoms (but keep  $\epsilon_{\text{ss}} = 1$  for icosahedron model excluder pseudoatoms).

### B. Hard sphere theory

To account for subunit excluded volume while computing  $K_{\text{c}}$ , we model subunits as effective hard spheres with diameter  $\sigma_1$ . At equilibrium, subunits in the condensate and background must have equal chemical potentials:

$$\mu_{\text{c}} = \mu_{\text{bg}}. \quad (\text{S10})$$

The chemical potentials can be written in terms of ideal and excess (hard sphere) components:

$$\mu_{\text{bg}} = \mu^{\text{ex}}(\rho_1^{\text{bg}}\sigma_1^3) + k_{\text{B}}T \log(\rho_1^{\text{bg}}\sigma_1^3) \quad (\text{S11a})$$

$$\mu_{\text{c}} = \mu^{\text{ex}}(\rho_1^{\text{c}}\sigma_1^3) + k_{\text{B}}T \log(\rho_1^{\text{c}}\sigma_1^3) - \epsilon_{\text{c}}. \quad (\text{S11b})$$

Within the Carnahan-Starling approximation,  $\mu^{\text{ex}}$  is given by [6]:

$$\mu^{\text{ex}}(\rho\sigma_1^3) = \frac{\eta(3\eta^2 - 9\eta + 8)}{(1 - \eta)^3}, \quad \eta = \frac{\pi}{6}\rho\sigma_1^3, \quad (\text{S12})$$

where  $\eta$  is the hard sphere packing fraction. Plugging Eqs. S11a, S11b in Eq. S10 and rearranging, we obtain:

$$\frac{\rho_1^c}{\rho_1^{\text{bg}}} = e^{\beta[\epsilon_c + \mu^{\text{ex}}(\rho_1^{\text{bg}}\sigma_1^3) - \mu^{\text{ex}}(\rho_1^c\sigma_1^3)]}. \quad (\text{S13})$$

Combined with the mass conservation condition

$$\rho_1^{\text{bg}} = (1 + V_r)\rho_T - V_r\rho_1^c, \quad (\text{S14})$$

Eq. S13 can be solved self-consistently to obtain  $\rho_1^c$  and, hence,  $K_c$ . We set  $\sigma_1 = 2.1$  (the ‘T’ pseudoatom diameter) for the dodecahedron subunits and  $\sigma_1 = 3$  (the side length) for the icosahedron subunits. As shown in Fig. 10, we obtain excellent agreement between this hard sphere approximation and results from simulations with  $\epsilon_{\text{ss}} = 0$  over a wide range of  $\epsilon_c$ . In contrast, ideal solution theory breaks down for  $\epsilon_c \gtrsim 4$  (with  $\rho_T = 4 \times 10^{-4}$ ), corresponding to a packing fraction of  $\approx 10\%$ .

### S3. EQUILIBRIUM ASSEMBLY THEORY

#### A. Ideal solution theory

Here, we summarize an equilibrium theory for assembly coupled to LLPS in the ideal solution limit (in which excluded volume is neglected). This theory was previously developed in Ref. [7], and a similar theory was presented in Ref. [8]. At equilibrium, intermediates are vanishingly rare [9] and thus we assume that subunits are either monomers or part of complete capsids containing  $N_{\text{cap}}$  subunits ( $N_{\text{cap}} = 12$  for dodecahedral capsids and  $N_{\text{cap}} = 20$  for icosahedral capsids). Both monomers and capsids can be located in the condensate or in the background. We denote the concentrations of capsids in the condensate and background as  $\rho_{\text{cap}}^c$ ,  $\rho_{\text{cap}}^{\text{bg}}$  respectively. Equilibrium implies that, within each phase (condensate and background), the monomer and (per subunit) capsid chemical potentials are equal, and that monomer and capsid chemical potentials are equal between phases:

$$\mu_1^{\text{bg}} = \mu_{\text{cap}}^{\text{bg}} \quad (\text{S15a})$$

$$\mu_1^c = \mu_{\text{cap}}^c \quad (\text{S15b})$$

$$\mu_1^{\text{bg}} = \mu_1^c \quad (\text{S15c})$$

$$\mu_{\text{cap}}^{\text{bg}} = \mu_{\text{cap}}^c, \quad (\text{S15d})$$

with  $\mu_1^{\text{bg}}$ ,  $\mu_1^c$ ,  $\mu_{\text{cap}}^{\text{bg}}$ , and  $\mu_{\text{cap}}^c$  as the monomer and (per subunit) capsid chemical potentials in the background and condensate, respectively. Within the ideal solution approximation, the chemical potentials are given by [10]:

$$\mu_1^{\text{bg}} = k_B T \log(\rho_1^{\text{bg}}\sigma_1^3) \quad (\text{S16a})$$

$$\mu_1^c = k_B T \log(\rho_1^c\sigma_1^3) - \epsilon_c \quad (\text{S16b})$$

$$\mu_{\text{cap}}^{\text{bg}} = k_B T \log(\rho_{\text{cap}}^{\text{bg}}\sigma_1^3)/N_{\text{cap}} + f_{\text{capsid}} \quad (\text{S16c})$$

$$\mu_{\text{cap}}^c = k_B T \log(\rho_{\text{cap}}^c\sigma_1^3)/N_{\text{cap}} + f_{\text{capsid}} - \epsilon_c. \quad (\text{S16d})$$

with  $f_{\text{capsid}}$  as the per-subunit Helmholtz free energy of capsid formation. Additionally, mass conservation yields the constraint:

$$(1 + V_r)\rho_T = V_r\rho_1^c + \rho_1^{\text{bg}} + N_{\text{cap}}V_r\rho_{\text{cap}}^c + N_{\text{cap}}\rho_{\text{cap}}^{\text{bg}}. \quad (\text{S17})$$

We solve Eqs. S15 and S17 self-consistently (see Mathematica Notebook 1 available on the Open Science Framework OSFHome: <https://osf.io/hq2y8/>) to yield the concentrations of monomers and capsids in the background and condensate, and hence the total equilibrium yield:

$$f_c^{\text{equil}} = \frac{N_{\text{cap}}}{\rho_T} \left( \frac{V_r}{1 + V_r} \rho_{\text{cap}}^c + \frac{1}{1 + V_r} \rho_{\text{cap}}^{\text{bg}} \right). \quad (\text{S18})$$

Following Ref. [7], we note that in the limit of large capsid size ( $N \gg 1$ ), the equilibrium yield can be written as:

$$f_c^{\text{equil}} = \begin{cases} 1 - \frac{\rho_{\text{CAC}}}{\rho_{\text{T}}}, & \rho_{\text{T}} \gg \rho_{\text{CAC}} \\ \left(\frac{\rho_{\text{T}}}{\rho_{\text{CAC}}}\right)^N, & \rho_{\text{T}} \ll \rho_{\text{CAC}}, \end{cases} \quad (\text{S19})$$

with the critical assembly concentration:

$$\rho_{\text{CAC}} = \frac{1 + K_c V_r}{K_c (1 + V_r)} \left(\frac{1 + V_r}{V_r}\right)^{1/N} \rho_{\text{CAC}}^0, \quad (\text{S20})$$

and  $\rho_{\text{CAC}}^0$  as the critical assembly concentration without LLPS:

$$\rho_{\text{CAC}}^0 = N^{-1/N} e^{f_{\text{capsid}}/k_B T}. \quad (\text{S21})$$

Ideal solution theory thus predicts that increasing  $K_c$  and decreasing  $V_r$  reduce  $\rho_{\text{CAC}}$ . For the dodecahedron model, we set  $f_{\text{capsid}} = -5k_B T$  for  $\epsilon_{\text{ss}} = 6$  (see SI Section S4B for details on this estimate).

### B. Hard sphere theory

We now extend ideal solution theory to account for excluded volume. As in the ideal solution theory, at equilibrium we will have equality of chemical potentials between phases and between monomers and capsids within each phase (Eq. S10). To account for excluded volume, we model monomers and capsids as hard spheres with diameters  $\sigma_1$  and  $\sigma_{\text{cap}}$ , respectively. The chemical potentials are now given by:

$$\mu_1^{\text{bg}} = k_B T \log(\rho_1^{\text{bg}} \sigma_1^3) + \mu_1^{\text{ex}}(\rho_1^{\text{bg}}, \rho_{\text{cap}}^{\text{bg}}) \quad (\text{S22a})$$

$$\mu_1^{\text{c}} = k_B T \log(\rho_1^{\text{c}} \sigma_1^3) + \mu_1^{\text{ex}}(\rho_1^{\text{c}}, \rho_{\text{cap}}^{\text{c}}) - \epsilon_c \quad (\text{S22b})$$

$$\mu_{\text{cap}}^{\text{bg}} = k_B T \log(\rho_{\text{cap}}^{\text{bg}} \sigma_1^3)/N_{\text{cap}} + \mu_{\text{cap}}^{\text{ex}}(\rho_1^{\text{bg}}, \rho_{\text{cap}}^{\text{bg}})/N_{\text{cap}} + f_{\text{capsid}} \quad (\text{S22c})$$

$$\mu_{\text{cap}}^{\text{c}} = k_B T \log(\rho_{\text{cap}}^{\text{c}} \sigma_1^3)/N_{\text{cap}} + \mu_{\text{cap}}^{\text{ex}}(\rho_1^{\text{c}}, \rho_{\text{cap}}^{\text{c}})/N_{\text{cap}} + f_{\text{capsid}} - \epsilon_c. \quad (\text{S22d})$$

Here,  $\mu_1^{\text{ex}}$  and  $\mu_{\text{cap}}^{\text{ex}}$  are excess chemical potentials for a binary mixture of hard spheres [11, 12]:

$$\begin{aligned} \mu_{\nu}^{\text{ex}}(\rho_1, \rho_{\text{cap}}) = & c_0(\eta) + c_1(\eta) \frac{M_1 M_2}{M_3} \frac{\sigma_1}{M_1} + \left( c_1(\eta) \frac{M_1 M_2}{M_3} + 3a_2(\eta) \frac{M_2^3}{M_3^2} \right) \frac{\sigma_1^2}{M_2} \\ & + \left[ \eta c'_0(\eta) + (\eta c'_1(\eta) - c_1(\eta)) \frac{M_1 M_2}{M_3} + (\eta a'_2(\eta) - 2a_2(\eta)) \frac{M_2^3}{M_3^2} \right] \frac{\sigma_1^3}{M_3} \end{aligned} \quad (\text{S23a})$$

$$\eta = \frac{\pi}{6} (\rho_1 + \rho_{\text{cap}}) M_3 \quad (\text{S23b})$$

$$c_0(\eta) = -\log(1 - \eta) \quad (\text{S23c})$$

$$c_1(\eta) = \frac{3\eta}{1 - \eta} \quad (\text{S23d})$$

$$a_2(\eta) = \log(1 - \eta) + \frac{\eta}{(1 - \eta)^2} \quad (\text{S23e})$$

$$M_i = \frac{\sum_{\nu} \rho_{\nu} \sigma_{\nu}^i}{\sum_{\nu} \rho_{\nu}}, \quad (\text{S23f})$$

where  $\nu = 1, \text{cap}$  and the prime symbol denotes a derivative with respect to  $\eta$ .

We solve Eqs. S15 and S17 using the chemical potentials in Eq. S22 (see Mathematica Notebook 2 available on the Open Science Framework OSFHome: <https://osf.io/hq2y8/>) to obtain the equilibrium concentrations of monomers and capsids in each phase, and hence the equilibrium yield. For the dodecahedron model, we set  $\sigma_1 = 2.1$  (the ‘T’ pseudoatom diameter),  $\sigma_{\text{cap}} = 5.1$ , and  $f_{\text{capsid}} = -5k_B T$  (see SI Section S4A for details on estimating  $\sigma_{\text{cap}}$ ). We plot both the ideal solution and hard sphere predictions for  $f_c^{\text{equil}}$  versus  $\rho_{\text{T}}$  for different values of  $\epsilon_c$  in Fig. S1. For  $\epsilon_c = 0$  the ideal solution and hard sphere results closely match, as expected for a dilute solution. On the other hand, when a condensate is present ( $\epsilon_c > 0$ ), the hard sphere predictions deviate significantly from ideal solution theory beyond a threshold concentration, reflecting the high concentration of subunits within the condensate.

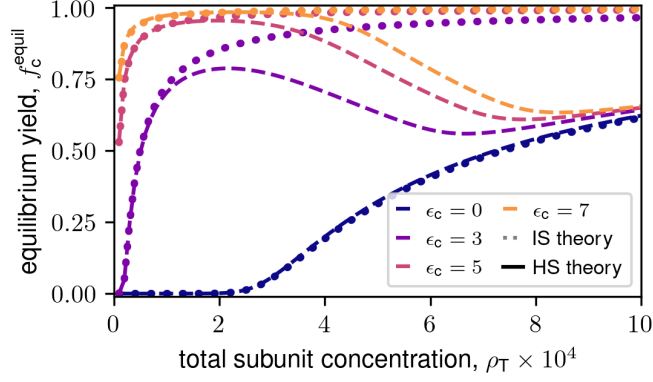


FIG. S1. Equilibrium yield versus total subunit concentration, predicted by the HS (solid lines) and IS (dotted lines) theories for indicated values of  $\epsilon_c$ . Parameters are: the subunit binding well depth  $\epsilon_{ss} = 6$ , and condensate volume fraction  $V_r = 5.0 \times 10^{-3}$ , and final simulation time  $t_F = 6 \times 10^5$ .

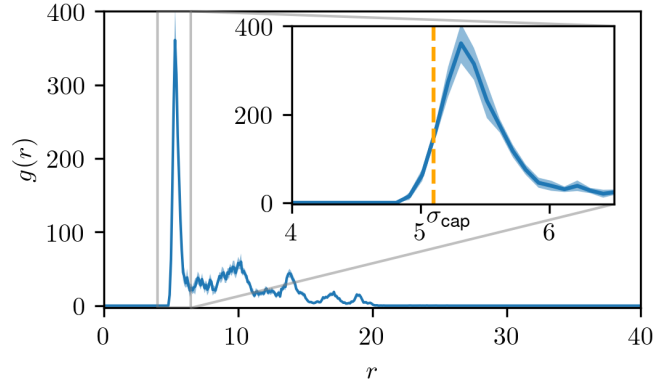


FIG. S2. Capsid radial distribution function  $g(r)$  versus center-of-mass distance  $r$ , computed from simulations with  $V_r = 5.0 \times 10^{-3}$ ,  $\rho_T = 10^{-3}$ ,  $\epsilon_{ss} = 6$ , and  $\epsilon_c = 7$ . Here  $g(r)$  was computed by averaging over the final configurations of 10 independent assembly trajectories, with error bars representing the standard error. The inset shows a zoomed-in view of the first peak, and the orange dashed line shows the capsid effective hard sphere diameter  $\sigma_{cap}$ .

## S4. ESTIMATING PARAMETERS FOR THE THEORETICAL MODEL

### A. Estimating $\sigma_{cap}$

To estimate the capsid effective hard sphere diameter, we computed the capsid radial distribution function  $g(r)$  (Fig. S2) at a parameter set where condensates are densely packed with capsids ( $\rho_T = 10^{-3}$ ,  $V_r = 5.0 \times 10^{-3}$ ,  $\epsilon_{ss} = 6$ ,  $t_F = 6 \times 10^5$ ). We took  $\sigma_{cap}$  to be halfway between the location of the first peak of  $g(r)$  ( $\approx 5.3$ ) and the smallest value of  $r$  for which  $g(r)$  is nonzero ( $\approx 4.9$ ), giving an estimate of  $\sigma_{cap} \approx 5.1$ . We also estimated  $\sigma_{cap}$  via an alternative route, in which we considered assembled capsids as rigid bodies and computed the minimum distance that two capsids could approach each other. In snapshots of densely packed capsids, we often observed capsids touching either face-to-face or vertex-to-face (with a ‘T’ pseudoatom on one capsid nestled between a face consisting of three ‘T’ pseudoatoms on another capsid). We therefore computed the distance of closest approach in either of these two orientations, obtaining values of  $\approx 4.8$  for face-to-face and  $\approx 5.3$  for vertex-to-face (see Mathematica Notebook 3 available on the Open Science Framework OSFHome: <https://osf.io/hq2y8/>). The average of these two values is approximately equal to our previous estimate of  $\sigma_{cap} \approx 5.1$ .

### B. Estimating $f_{\text{capsid}}$

To estimate  $f_{\text{capsid}}$ , we used previously reported approximate free energies for capsid intermediates up to, but not including, a full capsid in the dodecahedron model (see Ref. [13]). We plot these free energies for  $\epsilon_{\text{ss}} = 6$  in Fig. S3. For intermediate sizes  $n \gtrsim 3$ , the free energy to add an additional subunit is roughly independent of  $n$ ,  $\approx -5.5k_{\text{B}}T$ , until the 11th subunit binds. The accuracy of these free energy estimates is limited by sampling for larger intermediates and we would expect a more nonlinear dependence on  $n$  (since more bonds are formed on average as intermediates grow and the binding entropy is expected to be sub-linear in number of bonds [14, 15]). Furthermore, because the insertion of the 12th subunit (making a complete capsid) makes more bonds (5) compared to previous subunits than any other, this reaction is irreversible on simulation timescales. That is, we never see a complete capsid disassemble at binding energy values for which assembly occurs. Given the irreversibility and larger number of bonds formed, we anticipate that the free energy of adding the final subunit is significantly higher than that of adding previous subunits. We thus roughly approximate the free energy of adding the final subunit as  $-11k_{\text{B}}T$ , roughly twice that of adding previous subunits, such that the total capsid free energy is  $\approx -60k_{\text{B}}T$ . Thus, the free energy per subunit is  $f_{\text{capsid}} \approx -5k_{\text{B}}T$ . However, the capsid free energy will depend on  $\epsilon_{\text{ss}}$ . To estimate this dependence, we use the previously-reported [16] dependence of dimerization free energy on  $\epsilon_{\text{ss}}$ ,  $\sim -1.56\epsilon_{\text{ss}} + Ts$ , where  $s$  is the per-subunit entropy. Assuming that the capsid free energy depends on  $\epsilon_{\text{ss}}$  in the same way as the dimerization free energy, we thus write:

$$f_{\text{capsid}}(\epsilon_{\text{ss}}) = -1.56\epsilon_{\text{ss}} + Ts. \quad (\text{S24})$$

We then use the fact that  $f_{\text{capsid}}(6k_{\text{B}}T) = -5k_{\text{B}}T$  to obtain  $Ts = 4.36k_{\text{B}}T$ .

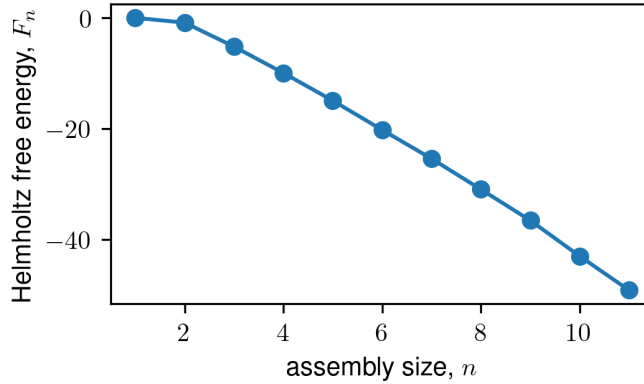


FIG. S3. Helmholtz free energy  $F_n$  as a function of assembly size  $n$ . Data taken from Ref. [16].

### S5. YIELD VS $\epsilon_{\text{ss}}$ AT DIFFERENT TIMES

Fig. S4a,b plots the yields from Fig. 6 at different times for  $\epsilon_c = 7$  and  $\epsilon_c = 0$  respectively. With LLPS, capsid production is orders of magnitude faster and yields approach much closer to the estimated equilibrium value within the finite simulation timescale. Moreover, assembly rates are increased even in conditions leading to malformed assemblies ( $\epsilon_{\text{ss}} \geq 7.5$ ). However, consistent with the results described in the main text, assembly growth slows at later times. While the slowdown with LLPS primarily occurs due to the excluded volume effects described above, assembly rates in bulk solution decrease as monomers are depleted, leading to a growth in the size of the critical nucleus size and the associated free energy barrier [17].

### S6. SCALING THEORY FOR ASSEMBLY KINETICS

The kinetics of LLPS-mediated assembly involves diffusion of subunits into the condensate, formation of critical nuclei, and elongation (growth) of nuclei into complete capsids. Previous work [7] predicted how LLPS affects the maximum assembly rate and median assembly timescale by noting that nucleation is typically the rate-limiting step in self-assembly, and by assuming that the primary effect of LLPS is to increase the nucleation rate by increasing

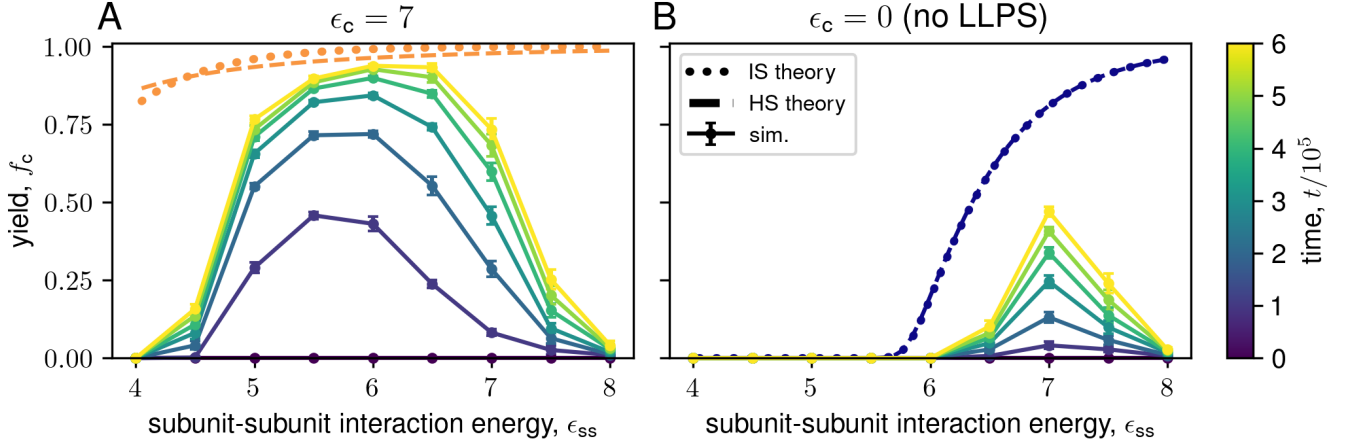


FIG. S4. Yield as a function of  $\epsilon_{ss}$  at indicated times for (A)  $\epsilon_c = 7$  and (B)  $\epsilon_c = 0$  (i.e. without LLPS), for the same parameters as Fig. 6A. The equilibrium hard sphere and ideal solution theories are shown as dashed and dotted lines respectively.

the local subunit concentration. Also assuming that the critical nucleus size  $n_{\text{nuc}}$  is independent of conditions, the maximum assembly rate  $r_{\text{max}}$  and median assembly time  $\tau_{1/2}$  were predicted to depend on the partition coefficient  $K_c$  and condensate volume fraction  $V_r$  as:

$$\begin{aligned}
 r_{\text{max}}(V_r, K_c) &\approx r_{\text{nuc}}(V_r, K_c) = s_{\text{nuc}} r_{\text{nuc}}^0 \\
 \tau_{1/2}(V_r, K_c) &= \tau_{1/2}^0 / s_{\text{nuc}} \\
 s_{\text{nuc}} &= \left( \frac{1 + V_r}{1 + K_c V_r} \right)^{n_{\text{nuc}}} \frac{1 + V_r K_c^{n_{\text{nuc}}}}{1 + V_r} \\
 &\approx V_r / (V_r + 1/K_c)^{n_{\text{nuc}}}.
 \end{aligned} \tag{S25}$$

Here,  $r_{\text{nuc}}^0$  and  $\tau_{1/2}^0$  are the initial nucleation rate (before significant subunit depletion has occurred) and median assembly time in the absence of LLPS ( $\epsilon_c = 0$ ). The approximate expression for the nucleation speedup  $s_{\text{nuc}}$  is valid for  $K_c^{n_{\text{nuc}}} \gg 1/V_r$ , such that nucleation occurs only in the compartment.

This previously-developed scaling theory assumes diffusion is very fast compared to nucleation. Yet this assumption is violated in our simulations, particularly for high  $\epsilon_c$ , as shown in Fig. 7C,F in the main text. We therefore extend the scaling theory to account for diffusive timescales. First, we note that the maximum assembly rate will be limited by the diffusive flux of subunits into the condensate, (assuming that assembly occurs exclusively within the condensate) with a “forward” rate (i.e. diffusion *into* the condensate) given by:  $4\pi R_c D \rho_1^{\text{bg}}$  ( $\approx 4\pi R_c D \rho_T$ , assuming minimal subunit depletion). Second, we note that the median assembly time must account for the characteristic timescale for subunit diffusion between condensate and background (not just the forward flux of subunits into the compartment). To obtain this timescale, we follow the Supporting Material of Ref. [7] and write the dynamics of subunit partitioning between the background and compartment as:

$$\frac{d\rho_1^{\text{bg}}}{dt} = -\frac{4\pi R_c D}{V_c} \left( \rho_1^{\text{bg}} - \rho_1^c / K_c \right) \tag{S26a}$$

$$\frac{d\rho_1^c}{dt} = -\frac{V_c}{V_{\text{bg}}} \frac{d\rho_1^c}{dt}. \tag{S26b}$$

Assuming initial concentrations  $\rho_T$  in both the background and condensate results in:

$$\rho_1^c(t) = \left( \frac{1 + V_r}{V_r + 1/K_c} \right) \rho_T + \left( 1 - \frac{1 + V_r}{V_r + 1/K_c} \right) \rho_T e^{-(4\pi R_c D (V_r + K_c^{-1}) / V_c) t} \tag{S27}$$

We identify  $V_c / [(V_r + K_c^{-1}) 4\pi R_c D]$  as a diffusive timescale. However, this expression fails to account for the subunits that will form capsids. To roughly capture the diffusion timescale associated with those subunits, we add a term  $f_c V / (4\pi R_c D)$ , resulting in a total diffusive timescale:

$$\tau_D \approx \frac{V_c / (V_r + 1/K_c) + f_c V}{4\pi R_c D}, \tag{S28}$$



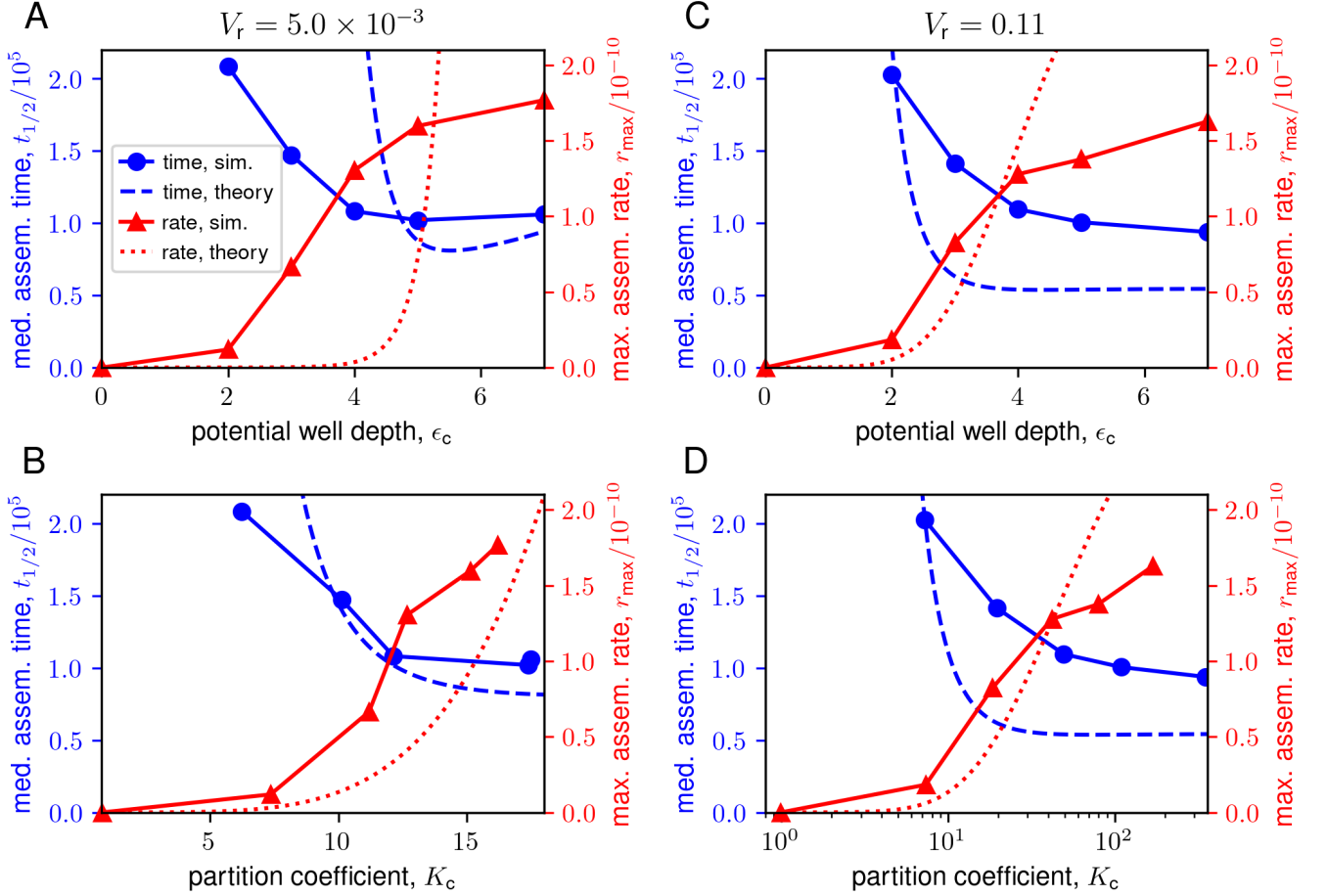


FIG. S5. Comparison of simulations and scaling theory for median assembly time  $\tau_{1/2}$  and maximum assembly rate  $r_{\max}$ . Panels A,B show results for  $V_r = 5.0 \times 10^{-3}$ , and panels C,D show results for  $V_r = 0.11$ . Panels A,C show results as a function of potential well depth  $\epsilon_c$ , while panels B,D show the same results as a function of partition coefficient  $K_c$ . The scaling theory curves (Eq. S25) were fit by eye to the simulation data for  $V_r = 0.11$  as a function of  $\epsilon_c$ , resulting in fitting parameters  $r_{\text{nuc}}^0 = 10^{-9}$ ,  $\tau_{1/2}^0 = 3 \times 10^7$ , and  $n_{\text{nuc}} = 5$ .

which is Eq. 5 in the main text. Thus, our new scaling estimates for  $r_{\max}$  and  $\tau_{1/2}$  are:

$$r_{\max}(V_r, K_c) = \frac{s_{\text{nuc}} r_{\text{nuc}}^0 4\pi R_c D \rho_T}{s_{\text{nuc}} r_{\text{nuc}}^0 + 4\pi R_c D \rho_T} \frac{\rho_T}{N_{\text{cap}}} \quad (\text{S29a})$$

$$\tau_{1/2}(V_r, K_c) = \tau_{1/2}^0 / s_{\text{nuc}} + \tau_D / 2. \quad (\text{S29b})$$

(We have included the factor of  $\rho_T / N_{\text{cap}}$  to give  $r_{\max}$  units of capsid concentration per unit time.)

We compare the theoretical predictions of Eq. S29 to simulation results in Fig. S5. Because we observe no assembly without LLPS for the parameters used in Fig. 7, we treat  $r_{\text{nuc}}^0$  and  $\tau_{1/2}^0$ , as well as  $n_{\text{nuc}}$ , as fitting parameters. We choose (by eye)  $r_{\text{nuc}}^0 = 10^{-9}$ ,  $\tau_{1/2}^0 = 3 \times 10^7$ , and  $n_{\text{nuc}} = 5$  to yield rough agreement with the simulation results for  $V_r = 0.11$ , and then use the same parameter values for  $V_r = 5 \times 10^{-3}$ . We find that the diffusive flux term  $4\pi R_c D \rho_T$  has little effect on  $r_{\max}$  because here  $4\pi R_c D \rho_T \gg s_{\text{nuc}} r_{\text{nuc}}^0$ ; however, we note that the true diffusive flux could be significantly smaller due to the excluded volume of subunits and capsids in the condensate “blocking” entry of additional subunits. However, including  $\tau_D/2$  in  $\tau_{1/2}$  correctly captures the saturation of  $\tau_{1/2}$  with  $\epsilon_c$  (without  $\tau_D$ , the theory severely underestimates the median assembly time at high  $\epsilon_c$ ).

When we assume the ideal solution partition coefficient ( $K_c^{\text{IS}} = e^{\beta \epsilon_c}$ ) and plot the scaling prediction as a function of  $\epsilon_c$  (Fig. S5A,C), we observe poor agreement, which worsens with increasing  $\epsilon_c$ , particularly for  $r_{\max}$ . However, we observe much better agreement when we instead use the values of  $K_c^{\text{meas}}$  measured at the time of maximum assembly rate for  $r_{\max}$  and at the median assembly time for  $\tau_{1/2}$  (Fig. S5B,D). The agreement particularly improves

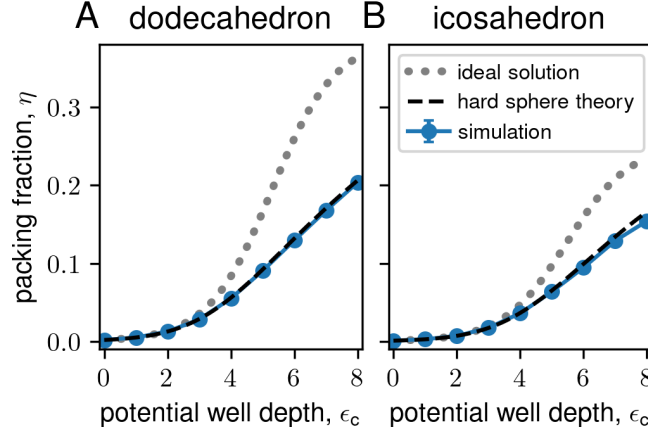


FIG. S6. Packing fraction in the condensate  $\eta = \frac{4}{3}\pi(\sigma_1/2)^3\rho_1^c$  as a function of potential well-depth  $\epsilon_c$  for the (A) dodecahedron model and (B) icosahedron model. Error bars are smaller than the size of the plotted points.

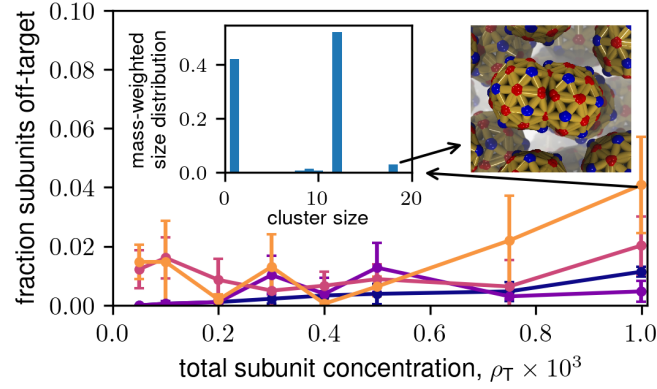


FIG. S7. Fraction of subunits in off-target structures (neither monomers nor capsids) versus total subunit concentration for different partition coefficients. The inset plot shows the mass-weighted cluster size distribution for  $\rho_T = 10^{-3}$ ,  $\epsilon_c = -7k_B T$ . The two largest peaks at cluster sizes of 1 and 12 correspond to monomers and capsids, respectively. The next largest peak is at 18, corresponding to partial capsids bound together as shown in the snapshot.

for  $V_r = 5 \times 10^{-3}$ , where the  $K_c^{\text{meas}}$  values deviate significantly from  $K_c^{\text{IS}}$ .

## S7. ADDITIONAL SUPPLEMENTARY FIGURES

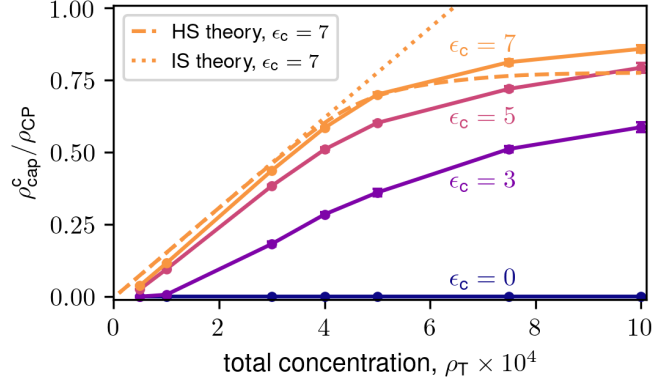


FIG. S8. Concentration of capsids in the condensate normalized by the estimated close-packing density,  $\rho_{\text{cap}}^c / \rho_{\text{CP}}$ , versus total subunit concentration for the same parameters as in Fig. 3.

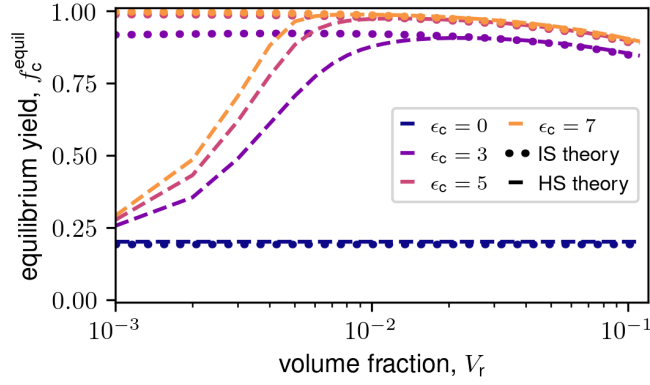


FIG. S9. Equilibrium yield versus volume fraction for indicated partition coefficient parameters, shown for the IS (dots) and HS (solid) theories. Parameters are  $\epsilon_{\text{ss}} = 6$ ,  $\rho_T = 4.00 \times 10^{-4}$ , and  $t_F = 6 \times 10^5$ .

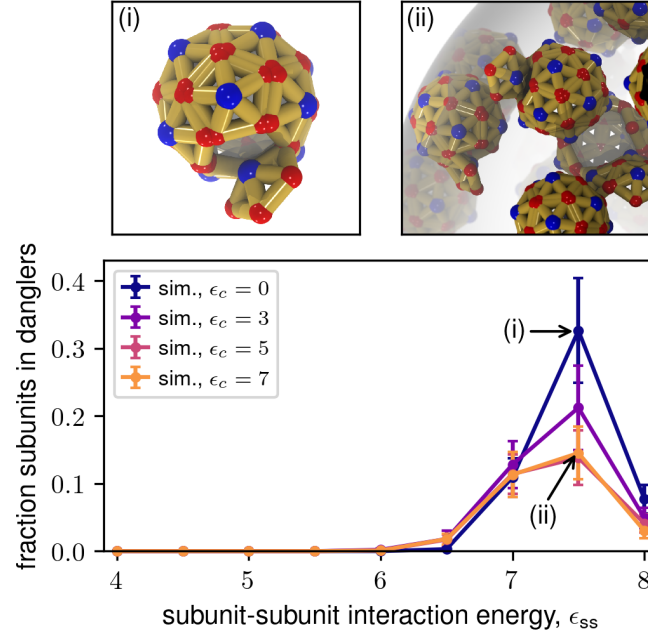


FIG. S10. Fraction of subunits in dangles versus subunit-subunit interaction energy. Snapshots above plot correspond to labeled points: (i) dangler in bulk solution with  $\epsilon_c = 0$  (ii) dangles in a condensate with  $\epsilon_c = 7$ . Parameters are:  $\rho_T = 4 \times 10^{-4}$ ,  $V_r = 5.0 \times 10^{-3}$ , and  $t_F = 10^6$

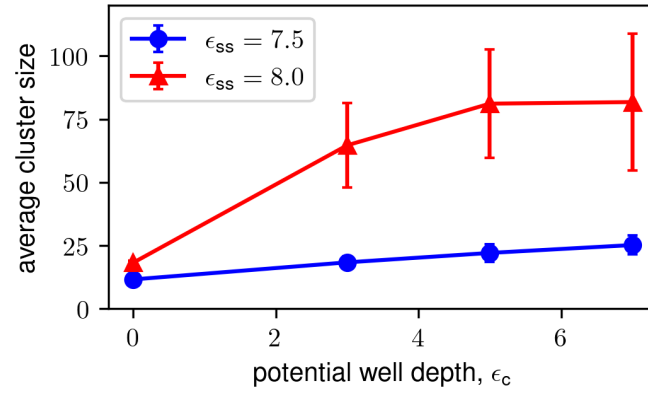


FIG. S11. The average cluster size at long times is shown as a function of  $\epsilon_c$  for  $\epsilon_{ss} = 7.5, 8$ . Parameters are:  $\rho_T = 4 \times 10^{-4}$ ,  $V_r = 5.0 \times 10^{-3}$ ,  $t_F = 6 \times 10^5$ .

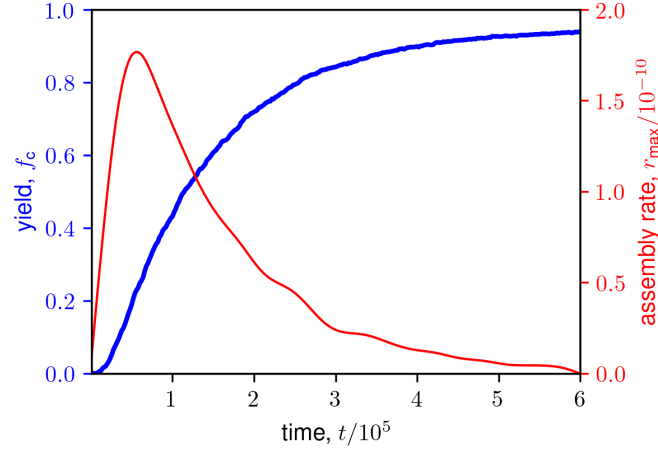


FIG. S12. Example of assembly rate calculation from yield vs. time data. The yield is the thick blue line; the assembly rate is the thin red line. The assembly rate is computed by convolving the yield curve with the derivative of a Gaussian; we set the smoothing parameter (i.e. the standard deviation of the Gaussian) to  $\sigma = 10$ . Simulation parameters are:  $\epsilon_c = 7$ ,  $\epsilon_{ss} = 6$ ,  $V_r = 5.0 \times 10^{-3}$ ,  $\rho_T = 4 \times 10^{-4}$ .

## S8. MOVIE DESCRIPTIONS

- **Movie S1:** Trajectory showing no assembly without LLPS. Parameters are:  $\epsilon_c = 0$ ,  $\epsilon_{ss} = 6$ ,  $\rho_T = 4 \times 10^{-4}$ .
- **Movie S2:** Capsid assembly trajectory without LLPS. Parameters are:  $\epsilon_c = 0$ ,  $\epsilon_{ss} = 7$ ,  $\rho_T = 4 \times 10^{-4}$ .
- **Movie S3:** Capsid assembly trajectory with LLPS for relatively weak subunit partitioning. Parameters are:  $\epsilon_c = 3$ ,  $\epsilon_{ss} = 6$ ,  $\rho_T = 4 \times 10^{-4}$ ,  $V_r = 5.0 \times 10^{-3}$ .
- **Movie S4:** Capsid assembly trajectory with LLPS for relatively strong subunit partitioning. Parameters are:  $\epsilon_c = 7$ ,  $\epsilon_{ss} = 6$ ,  $\rho_T = 4 \times 10^{-4}$ ,  $V_r = 5.0 \times 10^{-3}$ .
- **Movie S5:** Capsid assembly trajectory with LLPS for a relatively large condensate volume fraction. Parameters are:  $\epsilon_c = 7$ ,  $\epsilon_{ss} = 6$ ,  $\rho_T = 4 \times 10^{-4}$ ,  $V_r = 0.11$ .
- **Movie S6:** Capsid assembly trajectory without LLPS at high subunit binding affinity, exhibiting malformed structures. Parameters are:  $\epsilon_c = 0$ ,  $\epsilon_{ss} = 8$ ,  $\rho_T = 4 \times 10^{-4}$ .
- **Movie S7:** Capsid assembly trajectory with LLPS at high subunit binding affinity, exhibiting malformed structures. Parameters are:  $\epsilon_c = 7$ ,  $\epsilon_{ss} = 8$ ,  $\rho_T = 4 \times 10^{-4}$ ,  $V_r = 5.0 \times 10^{-3}$ .

- 
- [1] C. Sigl, E. M. Willner, W. Engelen, J. A. Kretzmann, K. Sachenbacher, A. Liedl, F. Kolbe, F. Wilsch, S. A. Aghvami, U. Protzer, M. F. Hagan, S. Fraden, and H. Dietz, Programmable icosahedral shell system for virus trapping, *Nature Materials* **20**, 1281 (2021).
  - [2] W.-S. Wei, A. Trubiano, C. Sigl, S. Paquay, H. Dietz, M. F. Hagan, and S. Fraden, Hierarchical assembly is more robust than egalitarian assembly in synthetic capsids, *Proceedings of the National Academy of Sciences* **121**, e2312775121 (2024).
  - [3] J. D. Weeks, D. Chandler, and H. C. Andersen, Role of Repulsive Forces in Determining the Equilibrium Structure of Simple Liquids, *The Journal of Chemical Physics* **54**, 5237 (1971).
  - [4] J. A. Anderson, J. Glaser, and S. C. Glotzer, HOOMD-blue: A Python package for high-performance molecular dynamics and hard particle Monte Carlo simulations, *Computational Materials Science* **173**, 109363 (2020).
  - [5] H. Kamberaj, R. J. Low, and M. P. Neal, Time reversible and symplectic integrators for molecular dynamics simulations of rigid molecules, *The Journal of Chemical Physics* **122**, 224114 (2005).
  - [6] P. Attard, Simulation of the chemical potential and the cavity free energy of dense hard-sphere fluids, *The Journal of Chemical Physics* **98**, 2225 (1993).
  - [7] M. F. Hagan and F. Mohajerani, Self-assembly coupled to liquid-liquid phase separation, *PLOS Computational Biology* **19**, e1010652 (2023).
  - [8] G. Bartolucci, I. S. Haugerud, T. C. T. Michaels, and C. A. Weber, The interplay between biomolecular assembly and phase separation, *eLife* **13**, 10.7554/eLife.93003.1 (2024).
  - [9] M. F. Hagan and G. M. Grason, Equilibrium mechanisms of self-limiting assembly, *Reviews of Modern Physics* **93**, 025008 (2021).
  - [10] J. N. Israelachvili, D. John Mitchell, and B. W. Ninham, Theory of self-assembly of hydrocarbon amphiphiles into micelles and bilayers, *Journal of the Chemical Society, Faraday Transactions 2: Molecular and Chemical Physics* **72**, 1525 (1976).
  - [11] G. A. Mansoori, N. F. Carnahan, K. E. Starling, and T. W. Leland, Equilibrium Thermodynamic Properties of the Mixture of Hard Spheres, *The Journal of Chemical Physics* **54**, 1523 (1971).
  - [12] D. M. Heyes and A. Santos, Chemical potential of a test hard sphere of variable size in a hard-sphere fluid, *The Journal of Chemical Physics* **145**, 214504 (2016).
  - [13] A. Trubiano, Self-Assembly Analysis Suite for HOOMD, <https://github.com/onehalfatsquared/SAASH> (2024).
  - [14] M. F. Hagan and D. Chandler, Dynamic pathways for viral capsid assembly, *Biophysical Journal* **91**, 42 (2006).
  - [15] M. F. Hagan, O. M. Elrad, and R. L. Jack, Mechanisms of kinetic trapping in self-assembly and phase transformation, *Journal of Chemical Physics* **135**, 104115 (2011).
  - [16] A. Trubiano and M. F. Hagan, Markov state model approach to simulate self-assembly, (2024).
  - [17] M. F. Hagan and O. Elrad, Understanding the concentration dependence of viral capsid assembly kinetics - the origin of the lag time and identifying the critical nucleus size, *Biophysical Journal* **98**, 1065 (2010).

# Computer simulations show that liquid-liquid phase separation enhances self-assembly

Layne B. Frechette,<sup>1,\*</sup> Naren Sundararajan,<sup>1,\*</sup> Fernando Caballero,<sup>1</sup> Anthony Trubiano,<sup>1</sup> and Michael F. Hagan<sup>1,†</sup>

<sup>1</sup>*Martin Fisher School of Physics, Brandeis University, Waltham, Massachusetts 02453, USA*

(Dated: May 27, 2025)

Biomolecular condensates are liquid- or gel-like droplets of proteins and nucleic acids formed at least in part through liquid-liquid phase separation. Condensates enable diverse functions of cells and the pathogens that infect them, including self-assembly reactions. For example, it has been shown that many viruses form condensates within their host cells to compartmentalize capsid assembly and packaging of the viral genome. Yet, the physical principles controlling condensate-mediated self-assembly remain incompletely understood. In this article we use coarse-grained molecular dynamics simulations to study the effect of a condensate on the assembly of icosahedral capsids. The capsid subunits are represented by simple shape-based models to enable simulating a wide range of length and time scales, while the condensate is modeled implicitly to study the effects of phase separation independent of the molecular details of biomolecular condensates. Our results show that condensates can significantly enhance assembly rates, yields, and robustness to parameter variations, consistent with previous theoretical predictions. However, extending beyond those predictions, the computational models also show that excluded volume enables control over the number of capsids that assemble within condensates. Moreover, long-lived aberrant off-pathway assembly intermediates can suppress yields within condensates. In addition to elucidating condensate-mediated assembly of viruses and other biological structures, these results may guide the use of condensates as a generic route to enhance and control self-assembly in human-engineered systems.

## I. INTRODUCTION

Many critical biological functions rely on high-fidelity assembly of structures, such as viral capsids [1–8], photonic nanostructures [9], bacterial microcompartments [10–17], and other proteinaceous organelles [18–22]. These structures form with astonishing robustness, despite the complex and highly adaptive nature of the cellular cytoplasm. Self-assembly also has promising technological applications, such as enabling highly scalable bottom-up manufacturing of nanostructured materials [23–25]. Recent developments in DNA origami, protein design, supramolecular assembly, and patchy-colloidal particles have enabled the design of human-engineered subunits that assemble into complex architectures including icosahedral shells and cylindrical tubules with programmable sizes (e.g. [26–67]). However, in contrast to biology, the ability to achieve high-fidelity assembly in these synthetic systems is far from robust, requiring precise tuning of subunit concentrations and interactions to avoid kinetic traps (long-lived off-pathway intermediates). [8, 31, 68–87]. Biological systems employ multiple mechanisms to avoid such kinetic traps. In this article we use computer simulations to investigate one of these mechanisms — self-assembly coupled to biomolecular condensates. Our results show that condensates can significantly increase assembly rates and robustness, and enable controlling the final yield.

It has become clear that biomolecular condensates formed through liquid-liquid phase separation (LLPS)

play a key role in spatially organizing cellular environments [88–92]. These ‘membraneless organelles’ are involved in essential processes, such as transcriptional regulation [93–97], cell division [98, 99], and neuronal synapse formation [100–102]. More recent evidence suggests that condensates can also control self-assembly within cells. Examples include the assembly of clathrin cages during endocytosis [103], the formation of post-synaptic densities [104] and pre-synaptic vesicle release sites [105, 106] at neuronal synapses, aggregation of  $\alpha$ -synuclein [107], and actin assembly in polypeptide coacervates [108]. In addition to normal biological functions, condensates are also critical for pathogenic infections. For example, in many viral infections, the outer protein shells (capsids) assemble within condensates known as virus factories, replication sites, Negri bodies, inclusion bodies, or viroplasms [109–128]. However, the effects of LLPS on assembly and the benefits to the viral lifecycle remain incompletely understood.

Extensive theoretical and computational works have investigated how condensates form and how they are controlled by chemical reactions and other nonequilibrium processes (e.g. [95, 96, 130–167]). However, there have been comparatively few studies of condensate-coupled assembly. Recent investigations using chemical kinetics-based rate equations suggest that preferential partitioning of subunits into condensates can significantly enhance assembly rates by locally concentrating the subunits [168, 169]. Ref. [169] also showed that LLPS can make assembly more robust to parameter variations, significantly broadening the range of subunit concentrations or binding affinities that lead to productive assembly. Although Bartolucci et al. [168] made a comprehensive study that included effects of subunits on condensate phase coexistence, in many systems the subunits remain

\* These two authors contributed equally.

† hagan@brandeis.edu

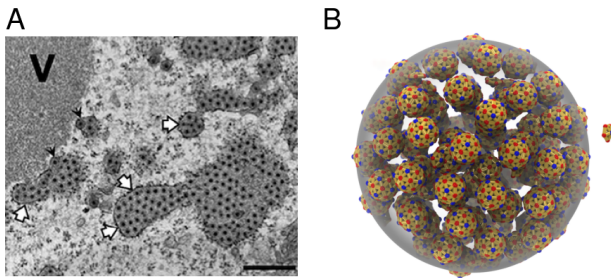


FIG. 1. Densely-packed viral factories in experiments and computer simulations. (A) Electron microscopy image from a rotavirus-infected cell. Gray regions are viroplasms, and black dots are assembled capsids. V, viroplasm; black arrowheads, enveloped viral particles; white arrows, endoplasmic reticulum surrounding viroplasms. Adapted from Papa et al. [129], which is licensed under CC BY 4.0. (B) Snapshot from a computer simulation of LLPS-coupled capsid assembly, showing capsids (small spherical particles) densely packed within a condensate (large gray sphere).

sufficiently dilute within condensates so that their effects on condensate stability can be neglected (i.e., subunits are “clients” rather than “scaffolds” [170]). Despite the important insights from these works, they were limited to rate equation models that assume spatially uniform concentrations within condensates. Further, they must pre-assume the set of allowed assembly intermediates and thus have not considered the excluded volume geometries of assembly structures or the possibility of malformed structures and other off-pathway intermediates that can limit assembly of target structures (e.g. [3, 5, 8, 28, 69–73, 78–84, 171–185]).

In this article, we use molecular dynamics simulations to avoid these approximations. To enable conclusions that are independent of the molecular details of condensates and to simulate a wide range of lengths and timescales, we implicitly model the condensate. That is, we represent the condensate as a spherical region with an attractive field that drives partitioning of subunits into the condensate. The simulation results are consistent with many of the predictions of the rate equation models, such as enhanced yields, rates and robustness to parameter variations, but also identify behaviors that are not captured in rate equation models. For example, capsid yields are suppressed by kinetic traps due to aberrant off-pathway structures for strong subunit binding affinities. Capsid yields also drop precipitously when the concentration of subunits approaches the close-packing limit. We develop an equilibrium theory that recapitulates this behavior, indicating that this reduction in yield is at least partially thermodynamic in origin. In this limit, we observe para-crystalline arrays of nearly closely packed capsids, which are highly reminiscent of recent electron microscopy images of virus factories (Fig. 1). We show that capsid yields can be precisely controlled by the conden-

sate volume. In addition to shedding light on viral life-cycles, this suggests a strategy to achieve size-controlled crystalline arrays in synthetic assembly systems.

## II. MODEL AND METHODS

We use molecular dynamics to simulate  $N$  subunits in a cubic box with edge-length  $L$  and volume  $V = L^3$  (subject to periodic boundary conditions) at a temperature  $T$ . We study assembly across a range of total subunit concentrations  $\rho_T = N/V$ . We perform our simulations using the GPU-accelerated HOOMD-blue package [186] (v2.9.0 for the icosahedron model, v4.6.0 and v4.8.0 for the dodecahedron model).

To assess the generality of our results, we study two capsid models, which differ in complexity and in the size of the assembled structures. To reduce the computational cost of simulating high-frequency vibrational motions, both models represent capsid subunits as rigid bodies. In the first model (Fig. 2A-C), inspired by SV40 virus capsids [187, 188] pentagonal subunits (Fig. 2A) with circumradius  $l_0$  assemble into dodecahedral capsids (Fig. 2C). The subunits consist of a top (‘T’) pseudoatom that has repulsive interactions with other ‘T’ pseudoatoms, a bottom (‘B’) pseudoatom that has repulsive interactions with ‘T’ pseudoatoms to help prevent subunits from binding with upside-down configurations, and five attractor (‘A’) pseudoatoms located at the vertices of the pentagon that account for subunit-subunit attractions ((Fig. 2B and SI Section S1). The ‘T’ and ‘B’ interactions are represented by a WCA-like potential [189]. The ‘A’ pseudoatoms interact via a Morse potential, for which the well-depth parameter  $\epsilon_{ss}$  sets the subunit-subunit binding affinity, which we estimate in SI Section S4.

The second, more complex, model (Fig. 2D-F) is inspired by DNA origami assembly, and consists of triangular subunits (Fig. 2D) of diameter  $\approx 3\sigma$  (where  $\sigma$  is the diameter of the pseudoatoms comprising each subunit) that assemble into  $T = 1$  icosahedral capsids (Fig. 2F) [31]. These subunits consist of 45 excluder pseudoatoms that account for excluded volume via a WCA potential, and six attractor pseudoatoms which bind to complementary attractor atoms via a Lennard-Jones potential with well depth  $\epsilon_{ss}$  (see Fig. 2B and SI Section S1). We describe the models in detail in the Supporting Information (SI) Section S1.

### A. Condensate model

We model the condensate as a spherical region of radius  $R_c$  centered at the origin. The condensate imposes a



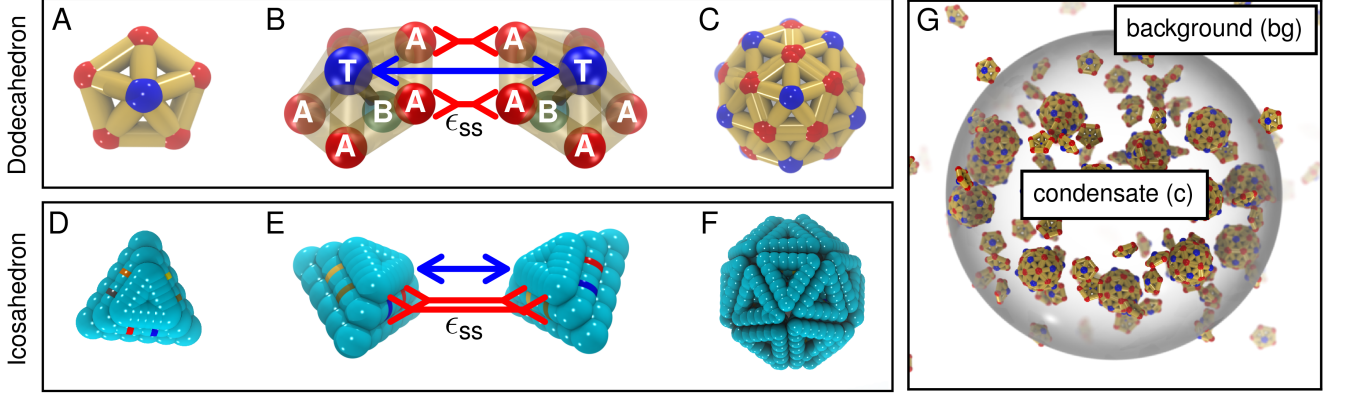


FIG. 2. Illustration of the capsid models. (A) Dodecahedron model subunit. (B) Interactions between dodecahedron subunits. Top ('T') pseudoatoms repel each other, while attractor ('A') pseudoatoms attract each other with interaction strength  $\epsilon_{ss}$ . Bottom ('B') pseudoatoms repel 'T' pseudoatoms, helping to prevent misbinding. (C) Dodecahedral capsid. (D) Icosahedron model subunit. (E) Interactions between icosahedron subunits. Excluder pseudoatoms (cyan) repel each other, while attractor pseudoatoms (all other colors) attract each other with interaction strength  $\epsilon_{ss}$ . (F) Icosahedral capsid. (G) Snapshot of a condensate containing monomeric subunits and capsids, taken from an assembly simulation of the dodecahedron model. Subunits can exchange between the condensate (gray sphere) with volume  $V_c$  and the background with volume  $V_{bg}$ . At equilibrium, the concentrations of monomers in the condensate and background are related by the partition coefficient,  $K_c = \rho_1^c / \rho_1^{bg}$ .

spherically symmetric potential given by:

$$u_c(r) = \begin{cases} -\epsilon_c, & r < R_c \\ -\epsilon_c (2e^{-2\alpha_c(r-R_c)} - e^{-2\alpha_c(r-R_c)}), & r \geq R_c \end{cases} \quad (1)$$

where  $r$  is the distance from the origin,  $\epsilon_c$  sets the depth of the potential well, and  $\alpha_c$  is a parameter that controls how rapidly the potential decays to zero as  $r$  increases beyond  $R_c$ . We set  $\alpha_c = 10 l_0^{-1}$  ( $10\sigma^{-1}$  for the icosahedron model), which ensures that the potential goes to zero over a length scale  $\alpha_c^{-1} \ll R_c$  while suppressing unphysically large forces at the condensate boundary. The condensate occupies a volume  $V_c$ , and the background has volume  $V_{bg} = V - V_c$ . We define the condensate volume ratio as  $V_r = V_c / V_{bg}$  to characterize the relative sizes of the condensate and background independently of the total volume. Except where otherwise noted, we use  $V_r = 5.03 \times 10^{-3}$  for the dodecahedron model and  $V_r = 4.20 \times 10^{-3}$  for the icosahedron model. These values are in the typical range for condensates within eukaryotic cells [92].

The well-depth  $\epsilon_c$  controls the strength of subunit-condensate interactions. For  $\epsilon_c > 0$ , subunits preferentially partition into the condensate, as characterized by the partition coefficient:

$$K_c = \frac{\rho_1^c}{\rho_1^{bg}}, \quad (2)$$

where  $\rho_1^c, \rho_1^{bg}$  are the equilibrium concentrations of unassembled subunits in the condensate and background (volume outside the condensate). In the ideal solution (IS) limit (for packing fractions  $\eta = \frac{\pi}{6} \rho l_0^3 \lesssim 0.1$ )

the partition coefficient is related to the well depth by  $K_c^{IS} = e^{\beta\epsilon_c}$ , and assembly will significantly increase partitioning of larger structures, since the driving force for a cluster with  $n$  subunits to partition into the condensate is  $\propto n\epsilon_c$ . However, for higher concentrations excluded volume effects will reduce the partition coefficient, particularly once capsids assemble due to their large excluded volume. We account for excluded volume effects of monomers alone (i.e. before assembly occurs) as well as in the presence of assembly by modeling subunits and capsids as effective hard spheres using the Carnahan-Starling equation of state [190, 191] and its extension to binary mixtures [192] (see Figs. 10, S6, and SI Section S2). See the Appendix for additional discussion of how  $K_c$  depends on  $\epsilon_c$ . A snapshot of a condensate containing both monomeric subunits and capsids is shown in Fig. 2G.

## B. Units

In both the dodecahedron and icosahedron models, the thermal energy  $k_B T$  (where  $k_B$  is Boltzmann's constant) serves as our unit of energy and the subunit mass  $m$  is the unit of mass. In the dodecahedron model,  $l_0$  is the unit length, and  $t_0 \equiv l_0 \sqrt{m/k_B T}$  is the unit time. For the icosahedron model,  $\sigma$  is the unit length and  $t_0 \equiv \sigma \sqrt{m/k_B T}$  is the unit time. We report all quantities in terms of these units (energies in  $k_B T$ , lengths in  $l_0$  for the dodecahedron model and  $\sigma$  for the icosahedron model, and times in  $t_0$ ).

### C. Simulation details

For the dodecahedron model, we use  $N = 1200$  subunits, and vary the box size from  $L = 288.5$  to  $106.3$  to control the concentration over the range  $\rho_T \in [5 \times 10^{-5}, 10^{-3}]$ . For the icosahedron model, we use  $L = 200$  and  $N = 149$  to  $2092$  to achieve  $\rho_T \in [1.8 \times 10^{-5}, 2.6 \times 10^{-4}]$ .

Trajectories are initialized with subunits placed in the box at random, non-overlapping positions. We then run Langevin dynamics for  $t_F = 10^6$  ( $1.2 \times 10^8$  time steps with time step  $\Delta t = 5 \times 10^{-3}$  for the dodecahedron model and  $2 \times 10^8$  time steps with  $\Delta t = 5 \times 10^{-3}$  for the icosahedron model) unless noted otherwise. All reported results were obtained by averaging over 10 (dodecahedron) or 5 (icosahedron) independent trajectories for each parameter set ( $\epsilon_{ss}$ ,  $\epsilon_c$ , and  $\rho_T$ ). Error bars represent twice the standard error of the mean (approximately a 95% confidence interval).

We used our open-source Python library SAASH [193] to analyze trajectories and calculate the yield of complete capsids. The library provides functions to identify fully assembled capsids as well as arbitrarily-sized clusters. For cluster identification, we consider two dodecahedron subunits to be bonded (and hence part of the same cluster) if the centers of the edges of two subunits are within 0.3 of each other; we consider two icosahedron subunits to be bonded if both pairs of attractor pseudoatoms on the two subunits are within 1.3 of each other. Additional Python scripts used in this work have been deposited on Github at the following URL: <https://github.com/Layne28/implicit-condensate>.

## III. RESULTS

### A. LLPS promotes robust assembly

In a uniform bulk solution, subunit concentration and binding affinity must be carefully tuned to achieve high yields (i.e. the fraction of subunits in complete capsids,  $f_c$ ) [77, 84, 194, 195]. Concentrations and binding affinities larger than their optimal values lead to kinetic traps, such as malformed assemblies or “monomer starvation” (in which many partial assemblies nucleate but do not form complete capsids due to rapid depletion of free monomers [69, 76, 77, 82]). On the other hand, concentrations and binding affinities that are too low result in nucleation times that exceed typical time scales of experiments or simulations. Our computational results illustrate these behaviors; in the absence of phase separation ( $\epsilon_c = 0$ ) we observe significant yields only in a narrow range of subunit-subunit interaction energies  $\epsilon_{ss}$  (Figs. 3, 4, 5, 6, and Supplementary Movies S1, S2). We define yield as the fraction of subunits in complete capsids, where a complete capsid for the dodecahedron or icosahedron model has 12 or 20 subunits respectively, and each subunit forms the maximum number of bonds

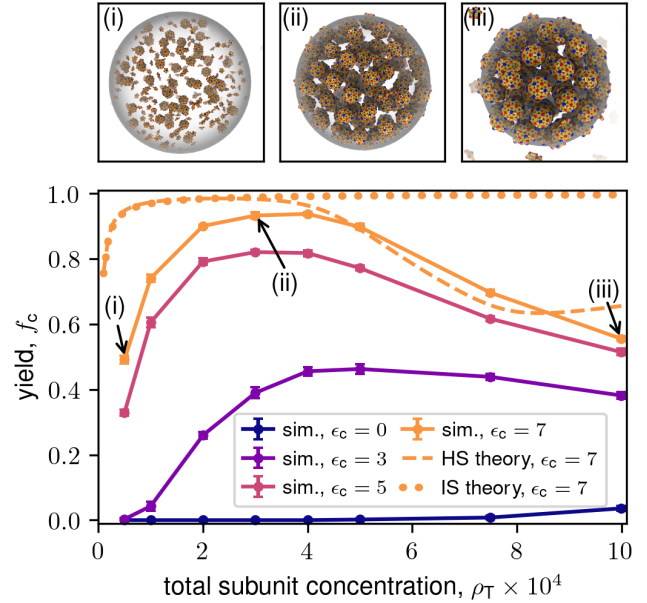


FIG. 3. Final capsid yield versus total subunit concentration  $\rho_T$  for the dodecahedron model for indicated values of  $\epsilon_c$ , which controls the partition coefficient  $K_c$ . Finite-time simulation yields are shown as symbols with lines. The hard sphere (HS) theory (dashed line) and ideal solution (IS) theory (dotted line) are shown for  $\epsilon_c = 7$ . Markers labeled (i-iii) correspond to snapshots above the plot. Parameters are: the subunit-subunit binding energy  $\epsilon_{ss} = 6$ , condensate volume fraction  $V_r = 5.0 \times 10^{-3}$ , and final simulation time  $t_F = 6 \times 10^5$ . Throughout this article, results are presented in dimensionless units defined in section II B. Except for Fig. 4, results are shown for the dodecahedron model.

(as defined in Section II C) with its neighbors, 5 or 3 respectively.

The computational results show that LLPS dramatically improves capsid assembly rates and yields in comparison to bulk assembly (Figs. 3, 4, 5, 6 and Supplementary Movies S3, S4, S5). While these trends are qualitatively consistent with rate equation models for assembly coupled to LLPS developed in Ref. [169], the computational model also exhibits important differences resulting from capsid excluded volume and off-pathway intermediates, which are not accounted for in the previous theory.

1. *There is an optimal subunit concentration due to capsid excluded volume.*

Figs. 3 and 4 show the long (but finite) time yields as a function of total subunit concentration ( $\rho_T$ ) for the dodecahedron and icosahedron models, along with representative simulation snapshots. Results are shown for several values of the partition coefficient for a relatively low binding affinity,  $\epsilon_{ss} = 6$ . While we observe almost no assembly in the absence of LLPS (see also Supplementary Movie S1), except for low yields at high  $\rho_T$ , LLPS leads

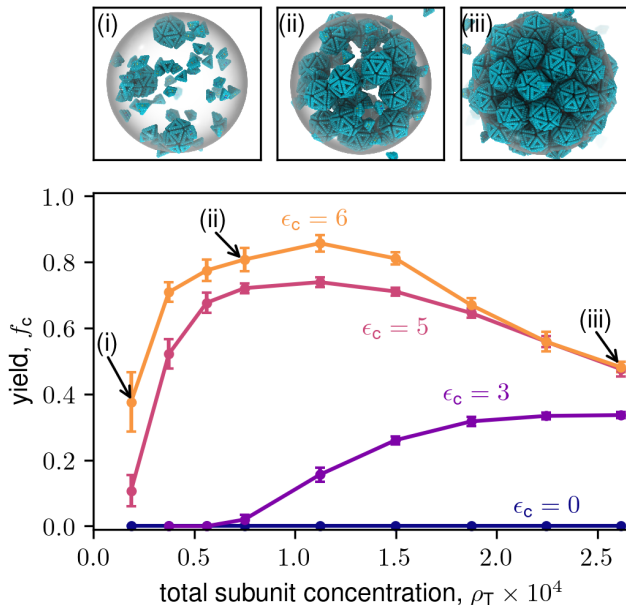


FIG. 4. Computational results for final capsid yield versus total subunit concentration for the icosahedron model for indicated values of  $\epsilon_c$ . Markers labeled (i-iii) correspond to snapshots above the plot. Parameters are:  $\epsilon_{ss} = 6$ ,  $V_r = 4.20 \times 10^{-3}$ , and  $t_F = 10^6$ .

to high yields over a wide range of concentrations. However, there is an optimal value of  $\rho_T$  beyond which yields decrease. For small partition coefficients, the optimal  $\rho_T$  decreases with increasing partition coefficient, but then seems to saturate; e.g. at  $\rho_T \approx 3 \times 10^{-4}$  for the dodecahedron model. Note that the saturation value depends on  $\epsilon_{ss}$  and  $V_r$ . The following analysis shows that these trends result from a combination of thermodynamic and kinetic effects.

First, we compare the simulation results against the equilibrium ideal solution theory from Ref. [169] (see SI Section S3 of this article). The dotted line in Fig. 3 shows the approximate equilibrium ideal solution result for the highest partition coefficient ( $\epsilon_c = 7$ ), and Fig. S1 shows results for different values of  $\epsilon_c$ . While qualitatively correct for low  $\rho_T$ , the ideal solution theory fails to capture the decrease in yields for large  $\rho_T$ . The ideal solution rate equation model also predicts high yields in this regime [169].

While previous simulation results in bulk solution exhibit such decreases in yield due to monomer starvation or malformed structures, we observe that almost all subunits are either monomers or part of assembled capsids for the entire range of  $\rho_T$  and  $K_c$ , with vanishingly few intermediates or malformed structures (see Fig. S7). Instead, we can explain the decrease in yield as a *thermodynamic* consequence of subunit excluded volume. For  $\rho_T \gtrsim 5 \times 10^{-4}$ , the concentration of assembled capsids within the condensate is roughly constant (Fig. S8), consistent with snapshots which show capsids densely packed

within condensates and no capsids in the background (see Figs. 3, 4). Capsids are near the close-packing limit, and hence the condensate cannot accommodate higher capsid concentrations as the total subunit concentration increases. These images are strikingly reminiscent of recent observations of rotavirus capsids closely packed in viroplasms (see 1).

Based on this observation, we developed a theory to predict the equilibrium capsid concentration, which accounts for subunits' excluded volume by approximating them as hard spheres (see SI Section S3). To briefly summarize the theory, we make the two-state approximation that subunits exist either as monomers or as part of assembled capsids. Equilibrium implies that the chemical potentials of monomers and capsids within each phase are equal, and that the chemical potentials of each species in the condensate and background phases are equal. Assuming that we can model monomer and capsid excluded volume by treating each of these species as effective hard spheres (whose diameters we estimate in SI Section S4), we estimate the chemical potentials using a standard hard sphere equation of state [192], and solve the resulting equations self-consistently to obtain the equilibrium concentrations of monomers and capsids in the condensate and background. The hard sphere theory results are shown (dashed line) for  $\epsilon_c = 7$  in Figs. 3, 4 and several values of  $\epsilon_c$  in Fig. S1. The theory correctly captures the non-monotonic dependence of yield on  $\rho_T$ , anticipates that the capsid concentration within the condensate saturates as  $\rho_T$  increases (Fig. S8), and predicts the optimal value of  $\rho_T$  to within a factor of 2 ( $\approx 2 \times 10^{-4}$  in theory vs  $\approx 4 \times 10^{-4}$  in simulations). For low  $\rho_T$  the theoretical yields are above the simulation results, which can be attributed to the fact that the simulation results are finite-time and thus smaller than equilibrium (assembly reactions approach equilibrium asymptotically slowly due to increasing nucleation barriers as subunits are depleted, see Fig. S4 and SI Section S5) [84, 196]) and that we only roughly estimate the subunit interaction free energy within capsids (see SI Section S4). The theory is less accurate, though still qualitatively good, at high  $\rho_T$  where capsid concentrations approach the close-packing limit (Fig. S8). We do not expect quantitative agreement in this regime because the Carnahan-Starling approximation significantly deviates from real hard-sphere behavior for  $\eta \gtrsim 0.5$  [191, 192]. Note that the slight increase in the theoretical yield at  $\rho_T \gtrsim 8 \times 10^{-4}$  arises due to assembly in the background, which we do not observe in simulations due to nucleation barriers.

Notably, there is a broad range of  $\rho_T$  over which the total concentration of assembled capsids  $\rho_{cap} \approx \rho_{cap}^c V_r$  is roughly constant, although at high enough concentrations (above the bulk critical subunit concentration ( $\rho_{CSC}$ ) capsids will also assemble in the background. Thus, condensates may provide a mechanism to control the total number of assembled capsids, since the number of capsids is bounded by the total condensate volume within this regime. Interestingly, optimal yields occur

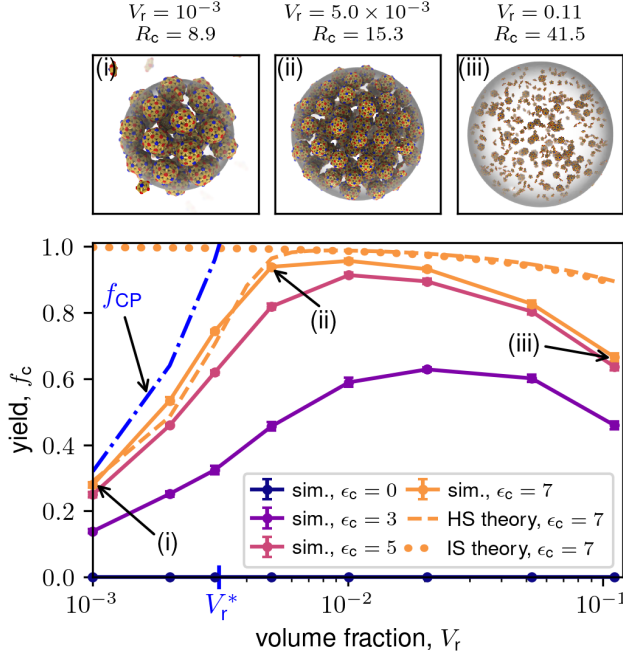


FIG. 5. Capsid yield versus condensate volume fraction for indicated values of  $\epsilon_c$  for the dodecahedron model. Finite-time simulation yields are shown as symbols with lines; the hard sphere theory (HS, dashed line) and ideal solution theory (IS, dotted line) predictions are shown for  $\epsilon_c = 7$ . Points labeled with Roman numerals correspond to snapshots above. Supplementary Movie S5 shows the trajectory from which snapshot (iii) was taken. The value  $V_r^*$ , marked in blue on the  $x$  axis, is the threshold volume fraction below which the close-packed yield theory (see section III A 1) predicts a decline in equilibrium yield. The estimated highest possible yield  $f_{CP}$  (Eq. 4, corresponding to spheres with approximately the size of capsids at close-packing density) is shown by the blue dash-dot line. Parameters are  $\epsilon_{ss} = 6$ ,  $\rho_T = 4.00 \times 10^{-4}$ , and  $t_F = 6 \times 10^5$ .

for capsid concentrations slightly below the close-packing limit,  $\rho_{cap}^c/\rho_{CP} \approx 0.6$ . This observation reflects thermodynamic costs (low translational entropy of capsids) and kinetic factors (slow subunit diffusion and hence assembly rates) at the close-packing limit.

## 2. There is an optimal condensate volume fraction due to capsid excluded volume.

The simulation yields also depend nonmonotonically on the condensate volume fraction  $V_r$  (Fig. 5), with an optimal value of  $V_r^*$  that decreases with  $\epsilon_c$ , and a sharp decrease in yields and finite-time yield for  $V_r \lesssim 5 \times 10^{-3}$ . This behavior is nearly quantitatively captured by the hard sphere theory for high  $\epsilon_c$ , but not by ideal solution theory, which predicts that yields increase monotonically with decreasing  $V_r$  (see Fig. S9 for theoretical predictions at different  $\epsilon_c$ ). The origin of this behavior is evident

from simulation snapshots, which show that the condensate becomes highly packed with assembled capsids for high  $\epsilon_c$  and low  $V_r$ .

In fact, the yields in this regime and the point corresponding to the steep decline can be qualitatively estimated from a simple sphere packing argument. Although the capsids have dodecahedral symmetry, they have a rounded shape and thus we treat them as effective spheres rather than faceted polyhedra in the following argument. Neglecting free monomers under the assumption of high yield, the maximum number of subunits that can form capsids within a condensate is  $N_{max} \approx N_{cap} V_c \rho_{CP}$ , where  $\rho_{CP}$  is the capsid close-packing concentration:

$$\rho_{CP} = \pi/(3\sqrt{2})/(4\pi(\sigma_{cap}/2)^3/3) \approx 1.28 \times 10^{-2} \quad (3)$$

where the capsid excluded volume size  $\sigma_{cap} = 5.1$  is estimated in SI Section S4A. Thus, below a threshold volume fraction  $V_r^*$  the total number of subunits exceeds the maximum number in the condensate  $N = V\rho_T > N_{max}$  and the yield declines (assuming assembly only occurs in the condensate). The threshold is  $V_r^* \approx 1/\left(\frac{N_{cap}\rho_{CP}}{\rho_T} - 1\right)$ , and the corresponding yield for  $V_r \leq V_r^*$  is

$$f_{CP} = \frac{(V_r^*)^{-1} + 1}{V_r^{-1} + 1}. \quad (4)$$

We plot  $f_{CP}$  in Fig. 5 and indicate the value of  $V_r^*$  ( $\approx 2.61 \times 10^{-3}$ ). The theory qualitatively matches the simulation results, although the decline occurs at slightly larger  $V_r$  in both finite-time simulation results and the equilibrium hard sphere theory. This agreement suggests that the simple packing argument explains the decline in yield at low  $V_r$ , but that assembly driving forces are not strong enough to reach complete close-packing. Indeed, Fig. S8 shows that capsid concentrations appear to saturate below the close-packing density, reaching  $\rho_{cap}^c/\rho_{CP} \approx 0.8$  for  $\epsilon_c = 7$ ,  $\rho_T = 10^{-3}$ .

## 3. There is an optimal binding affinity due to nucleation barriers and malformed structures.

Fig. 6A shows the long-time yields as a function of the subunit binding affinity parameter  $\epsilon_{ss}$  for the dodecahedron model, along with representative simulation snapshots. We observe that LLPS significantly enhances yields, particularly at low  $\epsilon_{ss}$  for which we observe no assembly in the absence of phase separation. Notably, we even observe higher yields for binding affinities that lead to strong assembly without phase separation ( $\epsilon_{ss} = 7$ ; see Supplementary Movie S2). However, for  $\epsilon_{ss} > 7$  there is a sharp decrease in yields for all partition coefficients. In contrast to the case of high subunit concentration, this decline is not captured by the hard sphere theory (shown for  $\epsilon_c = 7$ ), indicating that it does not arise due to excluded volume. Instead, the discrepancies arise due



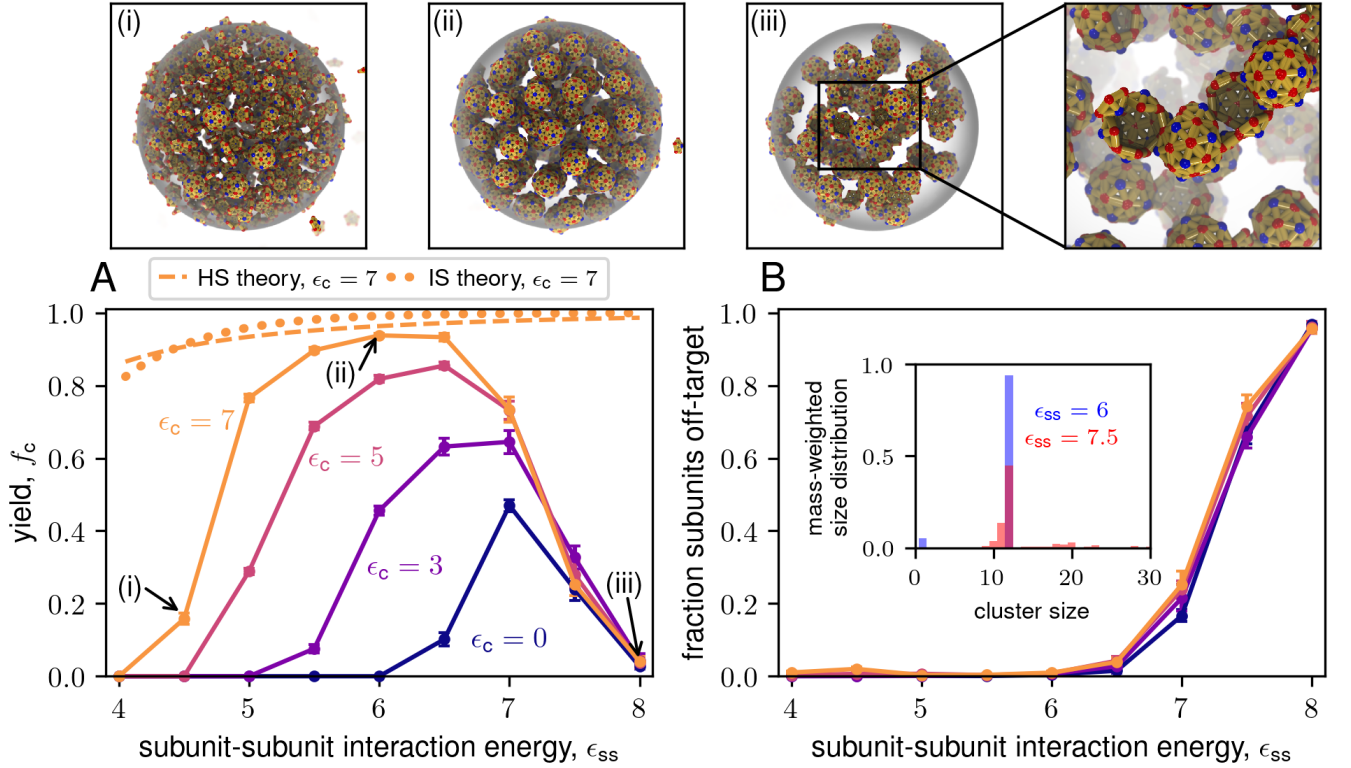


FIG. 6. (A) Yield as a function of the subunit binding affinity parameter ( $\epsilon_{ss}$ ) at indicated values of  $\epsilon_c$  for the dodecahedron model. Snapshots (i-iii) correspond to the labeled points at three different values of  $\epsilon_{ss}$  with  $\epsilon_c = 7$ . The inset in (iii) shows an example of a large, malformed assembly consisting of several half-shells bound together. See Supplementary Movie S7 for the trajectory corresponding to snapshot (iii). (B) Fraction of subunits in off-target structures as a function of  $\epsilon_{ss}$ . The inset shows the size distributions at  $\epsilon_{ss} = 6$  and  $\epsilon_{ss} = 7.5$ . Parameters for (A) and (B) are  $\rho_T = 4 \times 10^{-4}$  and  $V_T = 5.0 \times 10^{-3}$ .

to kinetic effects. For low binding affinities, nucleation barriers prevent reaching equilibrium within achievable simulation timescales. Since the nucleation barrier increases with decreasing binding affinity, the simulation results deviate further from equilibrium as  $\epsilon_{ss}$  decreases. However, as we discuss in section III B, LLPS has a significant effect on nucleation timescales.

In contrast, as the binding affinity increases beyond  $\epsilon_{ss} = 7$ , nucleation barriers are relatively small, but the prevalence of malformed off-pathway structures steadily increases (Fig. 6B). The appearance of malformed structures at strong binding affinity values is consistent with previous computational and experimental results from assembly in bulk solution [69, 74, 82, 84, 197–201]. Indeed, for  $\epsilon_{ss} \geq 7$ , we observe malformed structures (as well as assembled capsids) in both the background and the condensate (see Supplementary Movies S6, S7). However, Fig. 6 exhibits several notable features that highlight the interplay between malformed structures and LLPS-coupled assembly. First, the fraction of subunits in off-target structures is insensitive to  $\epsilon_c$ . This result is unexpected given the high local concentrations of subunits in the condensate, since high concentrations also favor the formation of malformed structures in bulk solu-

tion. Second, although the enhancement of yields is much greater for smaller binding affinities, LLPS enhances yields even within the malformed assembly regime. We attribute this enhancement to the ability of LLPS to prevent the monomer starvation trap, as discussed in Section III B. Third, the structures of malformed assemblies in the condensate differ from those in bulk solution. In bulk, malformed structures usually arise because subunits bind with incorrect geometries and are not significantly larger than well-formed capsids. For example, we commonly observe assemblies with 12 subunits but only 26 bonds. These “danglers” [202] (Fig. S10) form when the twelfth subunit binds in the wrong orientation; the unbinding is slow at high  $\epsilon_{ss}$ . In the condensate we observe fewer danglers (Fig. S10), but frequently see partially assembled capsids bound together to form large aggregates (snapshot (iii) in Fig. 6 and Supplementary Movie S7). This difference is reflected in a much larger average cluster size for  $\epsilon_{ss} \geq 7.5$  for LLPS-coupled assembly compared to  $\epsilon_c = 0$  (Fig. S11). We attribute these aggregates to the high local concentration of intermediates within the condensate under these conditions; binding of large intermediates to each other frequently leads to malformed structures [80].

## B. LLPS enhances assembly rates

In addition to enhancing long-time yields, LLPS also significantly increases assembly rates and thus the range of parameters leading to productive assembly at relevant timescales. Fig. 7A,C show the yield as a function of time for different values of  $\epsilon_c$  for moderate and large condensate volume fractions respectively ( $V_r = 5.0 \times 10^{-3}$  and 0.11), for fixed  $\epsilon_{ss} = 6$  and  $\rho_T = 4 \times 10^{-4}$ . Fig. 8A shows representative simulation snapshots at various times for  $\epsilon_c = 7, 3$ . While there is no assembly without LLPS ( $\epsilon_c = 0$ ) at these conditions, we observe rapid and productive assembly with LLPS. Rates increase dramatically with  $\epsilon_c$  for weak partitioning, but begin to level off for  $\epsilon_c > 3$ . More notably, the median assembly timescales  $\tau_{1/2}$  saturate at a minimum value of  $\tau_{1/2}^{\min} \approx 10^5$ .

To further quantify these trends, we plot the median assembly timescales and maximum assembly rates  $r_{\max}$  as a function of  $\epsilon_c$  for moderate and large condensate volume in Fig. 7B,D. We estimate the maximum assembly rate by convolving the assembly kinetics with the first derivative of a Gaussian (see Fig. S12). We consider the maximum assembly rate as an estimate of the initial nucleation rate because it eliminates the lag time required for a nucleus to grow into a complete capsid [196].

The observed acceleration of assembly rates with increasing  $\epsilon_c$  and decreasing  $V_r$  is consistent with the prediction from the rate equation theory [169]. However, the theory fails to capture the saturation of rates at high partitioning strength (see SI section S6 and Fig. S5).

The discrepancy between the ideal solution rate equation and the computational results arises because the interplay between assembly, capsid excluded volume, and subunit diffusion rates leads to a complex dynamics of subunit concentrations within the condensate for high  $\epsilon_c$  and low  $V_r$ . Fig. 8 shows the partition coefficient  $K_c^{\text{meas}}(t) = \rho_1^c(t)/\rho_1^{\text{bg}}(t)$  measured in simulations as a function of time for some of the parameter sets in Fig. 7. For large condensates ( $V_r = 0.11$ , Fig. 8C) subunits steadily partition into the condensate, reaching the equilibrium value of the partition coefficient by  $t = 2 \times 10^5$ . In contrast, for  $V_r = 0.005$  (Fig. 8B) and high  $\epsilon_c \gtrsim 4$ , subunit concentrations stall at  $K_c^{\text{meas}} \approx 10$ ; and then only gradually increase at later times. This is consistent with the observation that median assembly timescales saturate for  $\epsilon_c \gtrsim 4$ . Intriguingly though,  $K_c^{\text{meas}}$  overshoots the equilibrium value at early times for  $\epsilon_c = 3$ .

We can understand the results at low  $V_r$  as follows. Simulation trajectories show that assembly occurs extremely rapidly for low  $V_r$  and high partitioning  $\epsilon_c \gtrsim 7$  (see snapshot (v) in Fig. 8A), depleting subunits fast enough that the subunit flux from diffusion into the condensate ( $\approx 4\pi R D \rho_1^{\text{bg}}$  with  $D = k_B T / \gamma$  the subunit diffusion constant) cannot maintain the equilibrium partition coefficient (see Fig. 8B). Thus, the condensate reaches a quasi-steady-state where assembly rates are balanced by the subunit flux into the condensate, resembling previous models of assembly in the presence of monomer influx

([82, 203]). Then, as the condensate fills with capsids, the high excluded volume further slows subunit entry, leading to an extremely long timescale for subunit densities to reach equilibrium. In contrast, for weaker partitioning  $\epsilon_c \lesssim 3$ , nucleation in the condensate is sufficiently slow that subunit partitioning is unimpeded by capsid excluded volume at early times. Thus, subunit concentrations approach the equilibrium partition coefficient in the *absence* of capsid excluded volume (see Fig. 10), leading to the apparent overshoot. Then, as assembly proceeds, capsid excluded volume increases, and  $\rho_1^c$  decreases toward the equilibrium value.

These considerations show that for sufficiently strong partitioning, reaction rates will eventually be limited by the diffusive flux of subunits into the condensate. We can estimate the characteristic timescale for subunit diffusion into the condensate as (see SI section S6)

$$\tau_D \approx \frac{V_c/(V_r + 1/K_c) + f_c V_{\text{tot}}}{4\pi R_c D} \quad (5)$$

where the first and second terms in the numerator respectively account for diffusion of free subunits and those that eventually form capsids. As shown in Fig. 7,  $\tau_D/2$  (the cyan curve, with the factor of  $\frac{1}{2}$  because it is the median time) closely matches the minimum median assembly timescale for strong partitioning. Thus, subunit diffusion creates a speed limit on LLPS-facilitated assembly and thus a lower bound on assembly timescales.

**Implications for rate equation theory.** The above considerations show that the ideal solution rate equation theory needs to be extended to account for excluded volume effects as capsids accumulate in the condensate, which lead to reduced partition coefficients (as described in section II A) and slower subunit diffusion with correspondingly slower reaction rates.

In addition, we previously proposed a simple scaling estimate that LLPS accelerates nucleation rates and decreases assembly timescales by a factor (see Ref. [169] and SI section S6):

$$s_{\text{nuc}} \approx V_r / (V_r + 1/K_c)^{n_{\text{nuc}}} \quad \text{for } V_r \ll 1. \quad (6)$$

This estimate assumed an ideal solution, a critical nucleus size  $n_{\text{nuc}}$  that is independent of conditions, and that subunit diffusion is fast in comparison to assembly timescales so that the partition coefficient  $K_c$  maintains its equilibrium value. The simulations show that all these assumptions need to be relaxed at strong partitioning. We show in SI section S6 and Fig. S5 that this scaling estimate can be made to qualitatively match simulation results by using the measured values of the partition coefficient  $K_c^{\text{meas}}$  in  $s_{\text{nuc}}$ , and extending the expression for the median assembly timescale to include the diffusion timescale:

$$\tau_{1/2} \approx \tau_{1/2}^0 / s_{\text{nuc}} + \tau_D / 2 \quad (7)$$

with  $\tau_{1/2}^0$  the timescale in the absence of LLPS. Further effects that need to be accounted for include the fact that

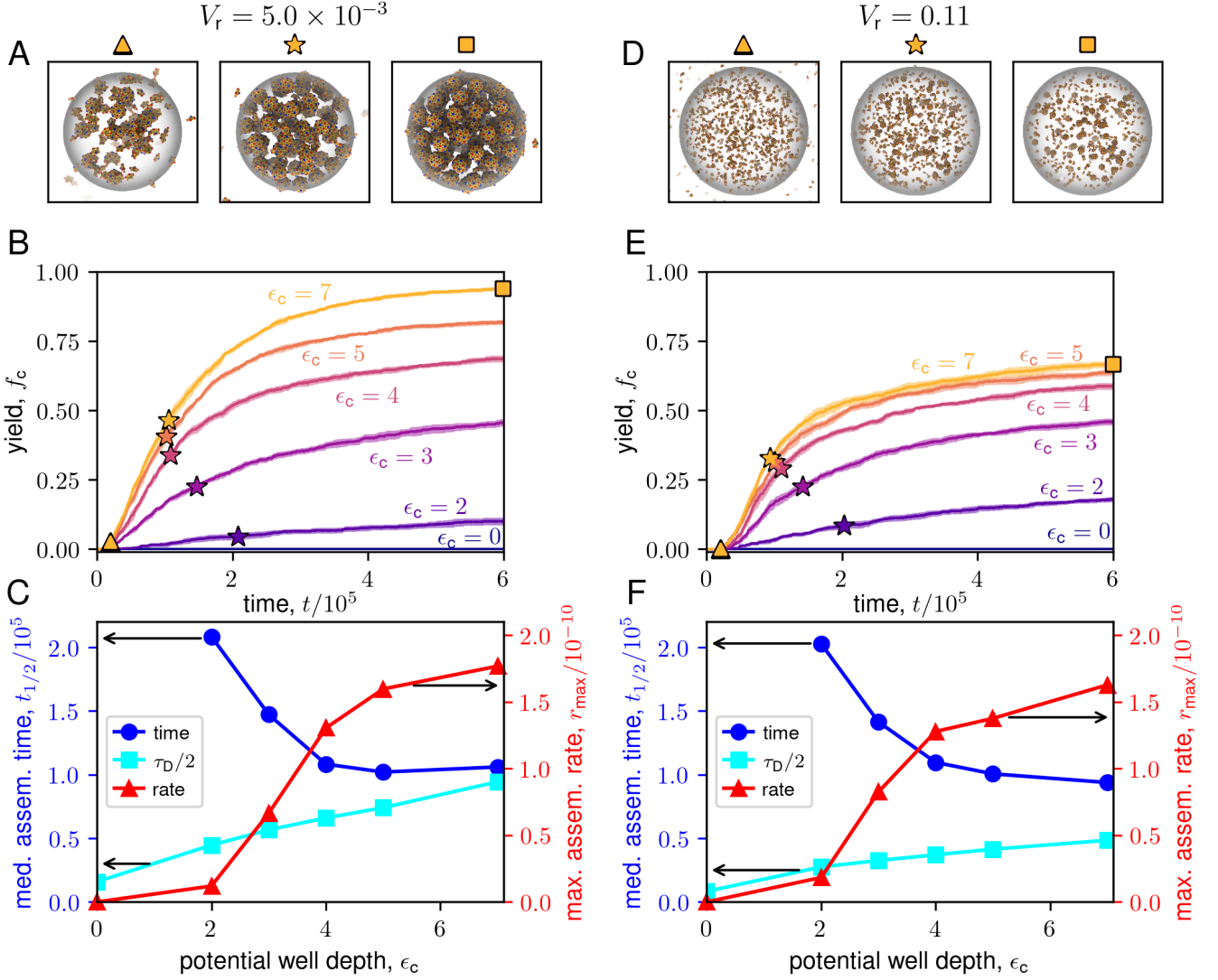


FIG. 7. LLPS-coupled assembly kinetics. The left column (panels A-C) shows results for  $V_r = 5.0 \times 10^{-3}$ , and the right column (panels D-F) shows results for  $V_r = 0.11$ . (A,D) Snapshots from assembly trajectories with  $\epsilon_c = 7$ , corresponding to times  $t/10^5 = 0.2, 1$ , and  $6$ , indicated by triangle, star, and square symbols on the plots in (B, E). See Supplementary Movies S4, S5 for the corresponding trajectories. (B,E) Yield versus time for different values of  $\epsilon_c$ . Stars indicate the median assembly times at all  $\epsilon_c$ . Parameters for both values of  $V_r$  are:  $\epsilon_{ss} = 6$ ,  $\rho_T = 4 \times 10^{-4}$ . (C,F) Median assembly time,  $\tau_{1/2}$  (blue, circles), and maximum assembly rate,  $r_{\max}$  (red, triangles), versus  $\epsilon_c$ . The solid cyan line with squares indicates half the diffusion time,  $\tau_D/2$  (Eq. (5)). Arrows indicate the  $y$  axis to which the lines correspond.

the critical nucleus size can decrease as local subunit concentrations increase and the above-mentioned decrease in reaction rates due to excluded volume.

**LLPS enables high rates by creating a buffer of free subunits.** By spatially localizing assembly within the condensate, LLPS enables extremely high assembly rates while limiting the overall rate of consuming subunits for  $V_r \lesssim 0.1$ . Under these conditions, the background solution acts as a “buffer” that steadily supplies free subunits to the condensate. This effect can avoid the monomer starvation kinetic trap, thus greatly increasing the possible rates and yields of assembly.

We quantify this mechanism by plotting the concentration  $\rho_1^{\text{bg}}$  of free subunits in the background as a function of the maximum assembly rate,  $r_{\max}$ , for different values of  $\epsilon_c$  over a range of  $\epsilon_{ss}$  (Fig. 9). Each data point in the plot corresponds to a different value of  $\epsilon_{ss}$  for the indicated  $\epsilon_c$  (shown in different colors). We see that for no LLPS ( $\epsilon_c = 0$ ),  $\rho_1^{\text{bg}}$  decreases rapidly with increasing  $r_{\max}$  (which is achieved by increasing  $\epsilon_{ss}$ ) because rapid nucleation throughout the entire simulation box depletes free subunits. In contrast, with LLPS ( $K_c > 1$ ),  $\rho_1^{\text{bg}}$  remains fairly close to  $\rho_T$  for assembly rates that are an order of magnitude higher, thus acting as a buffer.

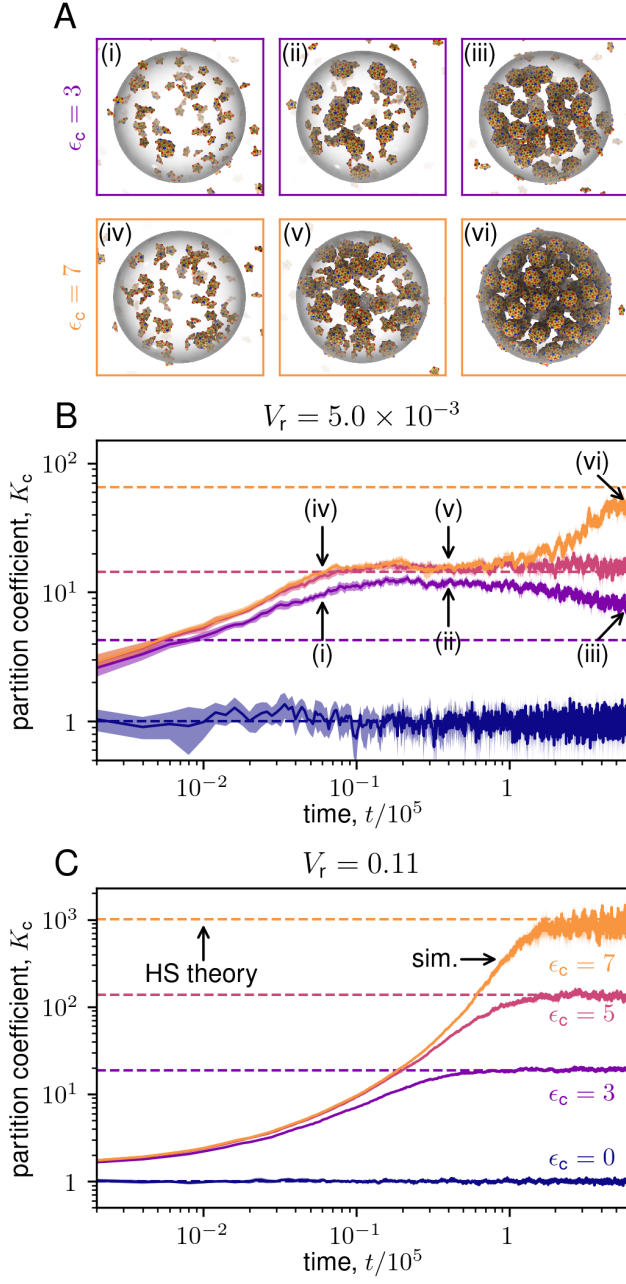


FIG. 8. Partitioning of subunits into condensate during assembly. (A) Snapshots from assembly trajectories for  $V_r = 5.0 \times 10^{-3}$  and  $\epsilon_c = 3$  (top) and 7 (bottom). See Supplementary Movies S3, S4 for segments of the corresponding trajectories. (B) Partition coefficient  $K_c^{\text{meas}}(t) = \rho_i^{\text{meas}}(t)/\rho_i^{\text{bg}}(t)$  measured in simulations as a function of time for indicated values of  $\epsilon_c$  at  $V_r = 5.0 \times 10^{-3}$ . Solid lines are  $K_c^{\text{meas}}(t)$ , and dashed lines are the predictions of HS theory. For  $\epsilon_c = 3$ ,  $K_c^{\text{meas}}$  initially rises well above the value of  $K_c$  appropriate for equilibrium between subunits and capsids, instead approaching the equilibrium value of  $K_c$  for no assembly (see Fig. 10). (C)  $K_c^{\text{meas}}(t)$  for indicated values of  $\epsilon_c$  at  $V_r = 0.11$ .

However, even with LLPS there is eventually a binding affinity above which the maximum rate decreases, due to assembly in the background solution, formation of malformed structures, or overly rapid assembly within the condensate.

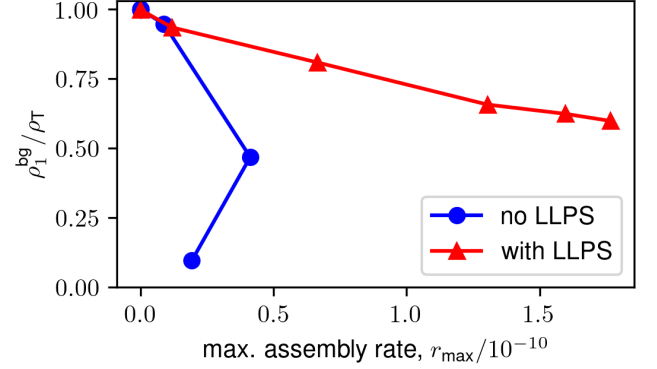


FIG. 9. The bulk solution acts as a buffer of free subunits with LLPS. The plot shows the background concentration  $\rho_1^{\text{bg}}$  (normalized by the total concentration  $\rho_T$ ) as a function of the maximum assembly rate both with (red, triangles) and without (blue, circles) LLPS. Each data point for “no LLPS” corresponds to a different value of  $\epsilon_{\text{ss}}$ , which ranges from  $4 \leq \epsilon_{\text{ss}} \leq 8$ , and  $\epsilon_c = 0$ . Each data point for “with LLPS” corresponds to a different  $\epsilon_c$ , with  $\epsilon_{\text{ss}} = 6$ .

#### IV. DISCUSSION

While these results are qualitatively consistent with previous rate equation models [168, 169], the particle-based simulations exhibit important differences due to excluded volume effects and aberrant off-pathway structures that are not accounted for in ideal solution theory and simplified rate equations. In particular, there is an optimal total subunit concentration  $\rho_T$  and condensate volume fraction  $V_r$ . For higher total subunit concentrations or lower condensate volumes, yields are limited by capsid excluded volume in the condensate. We developed an equilibrium theory for capsid assembly that includes these excluded volume effects, which agrees well with the simulation results. For higher-than-optimal binding affinity values, yields are suppressed by malformed off-pathway structures, independent of the subunit partition coefficient  $K_c$ . However, malformed structures form large aggregates within the condensate, while they tend to be on the order of the capsid size in bulk. In addition, we find that assembly rates are limited at high partition coefficients by the rate of subunit diffusion into the condensates. Rates are then further reduced by slow subunit diffusion once capsid excluded volume in the condensate becomes large. The latter effect is consistent with previous theoretical models [204, 205]. We show how the rate equation and associated scaling estimate for LLPS-



facilitated assembly rates and timescales [169] can be extended to include these effects.

*Diffusion sets a speed limit for LLPS-facilitated assembly.* For sufficiently strong partition coefficients, leading to high local subunit concentrations within the condensate, assembly rates can become limited by the diffusive flux of subunits into the condensate. The associated diffusive timescale sets a lower bound on the timescale for LLPS-facilitated assembly.

*Testing in experiments.* Our predictions on the dependence of yield and assembly rates on subunit concentrations and binding affinity values could also be tested in both biological and synthetic experiments in which self-assembly occurs within phase-separated condensates. In addition to viruses — the system that most closely motivates this work — our predictions could also be tested other cases described in the introduction (e.g. clathrin cages, actin filaments, and assemblies within neuronal synapses [103–108]). However, these predictions may be more readily tested in *in vitro* experiments which allow greater control over parameter values and condensate sizes, such as biomolecular assemblies [92, 102, 117, 206], or recently developed DNA origami subunits that form capsids and tubules [28, 29, 31, 32, 207].

The computational prediction that capsids fill phase-separated compartments to near close-packing densities under optimal assembly conditions are evocative of recent observations from cells infected with rotavirus [116, 123]. It would be of interest to investigate whether similar capsid arrays are observed in other viruses, what conditions give rise to such arrays, and more generally how capsid packing densities depend on parameter values.

*Implications for biology and synthetic assembly systems.* The ability of LLPS to increase assembly rates could be crucial for viruses to assemble before detection by host immune systems, and thus may be one reason why many viral systems form phase-separated compartments during their lifecycles. Further, while viruses have limited control over conditions within the host cell, they can control the partition coefficient and condensate volume. Faster assembly rates and enhanced control may also explain why many other biological assembly processes occur within condensates. In addition, the computational results show that there is a broad range of concentrations over which capsid concentrations within the condensate are nearly constant. Thus, by controlling the condensate volume, viruses can control the total number of assembled capsids. This might also provide a mechanism to control the timing of assembly — additional assembly would occur whenever capsids are released from the condensate.

Importantly, these same considerations suggest that LLPS could provide a means to enable rapid, robust assembly in human-engineered systems. In addition, our study identifies a route for efficient bottom-up assembly of highly monodisperse arrays of assemblies, which could have important optoelectronic applications. In contrast to previous approaches that can only assemble macro-

scopic crystals of capsids [208–210], condensate-coupled assembly enables precisely controlling the size of the crystalline arrays.

*Outlook.* The excluded volume effects identified in this work could be, at least approximately, accounted for in rate equation models following the approach that we have used for the equilibrium theory. Moreover, the theory can be applied to other assembly reactions occurring at high concentrations, such as the assembly of the mature HIV capsid [211–223]. Although our computational model accounts for this and other effects that were neglected in previous rate equation models, we have only implicitly modeled the condensate and assumed that the condensate phase coexistence is independent of subunit concentration. A natural next step is to explicitly model the constituents that form the condensate. This will allow studying the effect of subunits on condensate phase separation as well as additional effects that may arise from the excluded volume of condensate components.

## ACKNOWLEDGMENTS

This work was supported by the NSF through DMR 2309635 and the Brandeis Center for Bioinspired Soft Materials, an NSF MRSEC (DMR-2011846). Computing resources were provided by the National Energy Research Scientific Computing Center (NERSC), a Department of Energy Office of Science User Facility (award BES-ERCAP0026774); the NSF ACCESS allocation TGMCB090163; and the Brandeis HPCC which is partially supported by the NSF through DMR-MRSEC 2011846 and OAC-1920147.

## CONFLICTS OF INTEREST

The authors declare no conflicts of interest.

## DATA AVAILABILITY STATEMENT

Our simulation and analysis scripts are available on Github: <https://github.com/Layne28/implicit-condensate>. Additionally, post-processed trajectory data, Mathematica notebooks for theoretical calculations, and figure-generating scripts are hosted on the Open Science Framework OSFHome (<https://osf.io/hq2y8/>).

## Appendix A: Partition coefficient versus $\epsilon_c$

Fig. 10 shows the partition coefficient  $K_c$  as a function of potential well depth  $\epsilon_c$  for both capsid models at a single concentration with no assembly, and for the dodecahedron model with and without assembly over a range of concentrations.

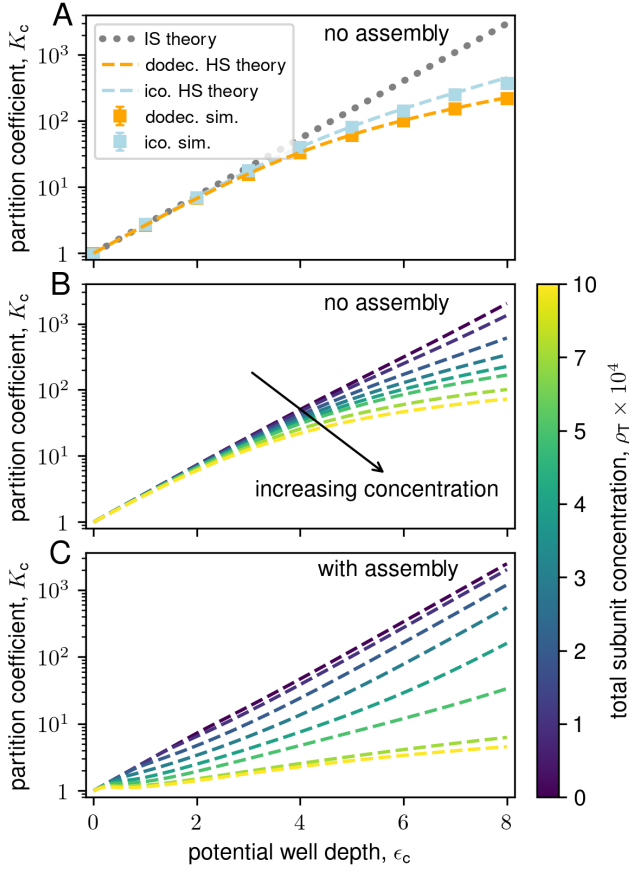


FIG. 10. Effects of excluded volume on the partition coefficient, with and without assembly. (A) Partition coefficient  $K_c$  versus condensate potential well depth  $\epsilon_c$  with no assembly (i.e. no subunit-subunit attractions,  $\epsilon_{ss} = 0$ ). The gray dotted line represents ideal solution (IS) theory. Orange and light blue represent results for the dodecahedron and icosahedron models, respectively, at concentrations  $\rho_T = 4 \times 10^{-4}$  (dodecahedron) and  $\rho_T = 7.5 \times 10^{-5}$  (icosahedron). The dashed lines represent the hard sphere (HS) theory using the Carnahan-Starling equation of state (see Section S2), and the square markers represent results from simulations with  $\epsilon_{ss} = 0$  (error bars are smaller than the size of the plotted points). In both cases, ideal solution theory breaks down when packing fractions in the condensate exceed  $\eta \gtrsim 10\%$  (Fig. S6). (B) Hard sphere theory results for the dodecahedron model without assembly over a range of concentrations. At the highest well depth and subunit concentration, excluded volume causes  $K_c$  to decrease by over an order of magnitude compared to ideal solution theory. (C) Hard sphere theory results for the dodecahedron model with assembly over a range of concentrations. At high concentrations, excluded volume causes  $K_c$  to decrease by orders of magnitude compared to ideal solution theory predictions.

[1] D. L. D. Caspar and A. Klug, Physical Principles in the Construction of Regular Viruses, Cold Spring Harbor Symposia on Quantitative Biology **27**, 1 (1962).

[2] A. Zlotnick and S. Mukhopadhyay, Virus assembly, allostery and antivirals, Trends in Microbiology **19**, 14 (2011).

- [3] M. G. Mateu, Assembly, stability and dynamics of virus capsids, *Archives of Biochemistry and Biophysics* **531**, 65 (2013).
- [4] R. F. Bruinsma and W. S. Klug, Physics of viral shells, *Annual Review of Condensed Matter Physics* **6**, 245 (2015).
- [5] J. D. Perlmutter and M. F. Hagan, Mechanisms of virus assembly, *Annual Review of Physical Chemistry*, Vol 62 **66**, 217 (2015).
- [6] M. F. Hagan and R. Zandi, Recent advances in coarse-grained modeling of virus assembly, **18**, 36 (2016).
- [7] R. Twarock, R. J. Bingham, E. C. Dykeman, and P. G. Stockley, A modelling paradigm for RNA virus assembly, **31**, 74 (2018).
- [8] R. Zandi, B. Dragnea, A. Travasset, and R. Podgornik, On virus growth and form, *Physics Reports-review Section of Physics Letters* (2020).
- [9] E. R. Dufresne, H. Noh, V. Saranathan, S. G. J. Mochrie, H. Cao, and R. O. Prum, Self-assembly of amorphous biophotonic nanostructures by phase separation, *Soft Matter* **5**, 1792 (2009).
- [10] A. A. D. T. Abeyasinghe, E. J. Young, A. T. Rowland, L. C. Dunshee, S. Urandur, M. O. Sullivan, C. A. Kerfeld, and C. D. Keating, Interfacial Assembly of Bacterial Microcompartment Shell Proteins in Aqueous Multiphase Systems, *Small* **20**, 2308390 (2024).
- [11] C. Chowdhury, S. Sinha, S. Chun, T. O. Yeates, and T. A. Bobik, Diverse Bacterial Microcompartment Organelles, *Microbiology and Molecular Biology Reviews* **78**, 438 (2014).
- [12] C. A. Kerfeld, S. Heinhorst, and G. C. Cannon, Bacterial Microcompartments, *Annual Review of Microbiology* **64**, 391 (2010).
- [13] C. A. Kerfeld and O. Erbilgin, Bacterial microcompartments and the modular construction of microbial metabolism, *Trends in Microbiology* **23**, 22 (2015).
- [14] C. A. Kerfeld and M. R. Melnicki, Assembly, function and evolution of cyanobacterial carboxysomes, *Current Opinion in Plant Biology* **31**, 66 (2016).
- [15] O. Erbilgin, K. L. McDonald, and C. A. Kerfeld, Characterization of a Planctomycetal Organelle: A Novel Bacterial Microcompartment for the Aerobic Degradation of Plant Saccharides, *Applied and Environmental Microbiology* **80**, 2193 (2014).
- [16] G. D. Price and M. R. Badger, Evidence for the role of carboxysomes in the cyanobacterial CO<sub>2</sub> -concentrating mechanism, *Canadian Journal of Botany* **69**, 963 (1991).
- [17] J. M. Shively, F. Ball, D. H. Brown, and R. E. Saunders, Functional Organelles in Prokaryotes: Polyhedral Inclusions (Carboxysomes) of *Thiobacillus neapolitanus*, *Science* **182**, 584 (1973).
- [18] M. Sutter, D. Boehringer, S. Gutmann, S. Gunther, D. Prangishvili, M. J. Loessner, K. O. Stetter, E. Weber-Ban, and N. Ban, Structural basis of enzyme encapsulation into a bacterial nanocompartment, *Nature Structural & Molecular Biology* **15**, 939 (2008).
- [19] R. J. Nichols, B. LaFrance, N. R. Phillips, L. M. Oltrogge, L. E. Valentin-Alvarado, A. J. Bischoff, E. Nogales, and D. Savage, Discovery and characterization of a novel family of prokaryotic nanocompartments involved in sulfur metabolism, *bioRxiv : the preprint server for biology* (2020).
- [20] F. Pfeifer, Distribution, formation and regulation of gas vesicles, *Nat Rev Micro* **10**, 705 (2012).
- [21] V. A. Kickhoefer, K. S. Rajavel, G. L. Scheffer, W. S. Dalton, R. J. Scheper, and L. H. Rome, Vaults are up-regulated in multidrug-resistant cancer cell lines, *Journal of Biological Chemistry* **273**, 8971 (1998).
- [22] B. Y. Zaslavsky, L. A. Ferreira, A. L. Darling, and V. N. Uversky, The solvent side of proteinaceous membraneless organelles in light of aqueous two-phase systems, *International Journal of Biological Macromolecules* **117**, 1224 (2018).
- [23] Z. Li, Q. Fan, and Y. Yin, Colloidal Self-Assembly Approaches to Smart Nanostructured Materials, *Chemical Reviews* **122**, 4976 (2022).
- [24] J. H. Fendler, Self-Assembled Nanostructured Materials, *Chemistry of Materials* **8**, 1616 (1996).
- [25] D. Vanmaekelbergh, Self-assembly of colloidal nanocrystals as route to novel classes of nanostructured materials, *Nano Today* **6**, 419 (2011).
- [26] P.W.K. Rothemund, Folding DNA to create nanoscale shapes and patterns, *Nature* **440**, 297 (2006).
- [27] E. Benson, A. Mohammed, J. Gardell, S. Masich, E. Czeizler, P. Orponen, and B. Högberg, DNA rendering of polyhedral meshes at the nanoscale, *Nature* **523**, 441 (2015).
- [28] C. Sigl, E. M. Willner, W. Engelen, J. A. Kretzmann, K. Sachenbacher, A. Liedl, F. Kolbe, F. Wilsch, S. A. Aghvami, U. Protzer, M. F. Hagan, S. Fraden, and H. Dietz, Programmable icosahedral shell system for virus trapping, *Nature Materials* **20**, 1281 (2021).
- [29] T. E. Videbæk, H. Fang, D. Hayakawa, B. Tyukodi, M. F. Hagan, and W. B. Rogers, Tiling a tubule: How increasing complexity improves the yield of self-limited assembly, *Journal of Physics: Condensed Matter* **34**, 134003 (2022).
- [30] D. Hayakawa, T. E. Videbæk, D. M. Hall, H. Fang, C. Sigl, E. Feigl, H. Dietz, S. Fraden, M. F. Hagan, G. M. Grason, and W. B. Rogers, Geometrically programmed self-limited assembly of tubules using DNA origami colloids, *Proceedings of the National Academy of Sciences* **119**, e2207902119 (2022).
- [31] W.-S. Wei, A. Trubiano, C. Sigl, S. Paquay, H. Dietz, M. F. Hagan, and S. Fraden, Hierarchical assembly is more robust than egalitarian assembly in synthetic capsids, *Proceedings of the National Academy of Sciences* **121**, e2312775121 (2024).
- [32] T. E. Videbæk, D. Hayakawa, G. M. Grason, M. F. Hagan, S. Fraden, and W. B. Rogers, Economical routes to size-specific assembly of self-closing structures, *Science Advances* **10**, eado5979 (2024).
- [33] K. F. Wagenbauer, C. Sigl, and H. Dietz, Gigadalton-scale shape-programmable DNA assemblies, *Nature* **552**, 78 (2017).
- [34] R. Divine, H. V. Dang, G. Ueda, J. A. Fallas, I. Vulovic, W. Sheffler, S. Saini, Y. T. Zhao, I. X. Raj, P. A. Morawski, M. F. Jennewein, L. J. Homad, Y.-H. Wan, M. R. Tooley, F. Seeger, A. Etemadi, M. L. Fahning, J. Lazarovits, A. Roederer, A. C. Walls, L. Stewart, M. Mazloomi, N. P. King, D. J. Campbell, A. T. McGuire, L. Stamatatos, H. Ruohola-Baker, J. Mathieu, D. Veessler, and D. Baker, Designed proteins assemble antibodies into modular nanocages, *Science* **372**, eabd9994 (2021).

- [35] G. L. Butterfield, M. J. Lajoie, H. H. Gustafson, D. L. Sellers, U. Nattermann, D. Ellis, J. B. Bale, S. Ke, G. H. Lenz, A. Yehdego, R. Ravichandran, S. H. Pun, N. P. King, and D. Baker, Evolution of a designed protein assembly encapsulating its own RNA genome, *Nature* **552**, 415 (2017).
- [36] J. B. Bale, S. Gonen, Y. Liu, W. Sheffler, D. Ellis, C. Thomas, D. Cascio, T. O. Yeates, T. Gonen, N. P. King, and D. Baker, Accurate design of megadalton-scale two-component icosahedral protein complexes, *Science* **353**, 389 (2016).
- [37] Y. Hsia, J. B. Bale, S. Gonen, D. Shi, W. Sheffler, K. K. Fong, U. Nattermann, C. Xu, P.-S. Huang, R. Ravichandran, S. Yi, T. N. Davis, T. Gonen, N. P. King, and D. Baker, Design of a hyperstable 60-subunit protein icosahedron, *Nature* **535**, 136 (2016).
- [38] N. P. King, W. Sheffler, M. R. Sawaya, B. S. Vollmar, J. P. Sumida, I. Andre, T. Gonen, T. O. Yeates, and D. Baker, Computational design of self-assembling protein nanomaterials with atomic level accuracy, *Science* **336**, 1171 (2012).
- [39] Q. M. Dowling, Y.-J. Park, N. Gerstenmaier, E. C. Yang, A. Wargacki, Y. Hsia, C. N. Fries, R. Ravichandran, C. Walkey, A. Burrell, D. Veessler, D. Baker, and N. P. King, Hierarchical design of pseudosymmetric protein nanoparticles, *bioRxiv*, 2023.06.16.545393 (2023).
- [40] A. D. Malay, N. Miyazaki, A. Biela, S. Chakraborti, K. Majsterkiewicz, I. Stupka, C. S. Kaplan, A. Kowalczyk, B. M. A. G. Piette, G. K. A. Hochberg, D. Wu, T. P. Wrobel, A. Fineberg, M. S. Kushwah, M. Kelemen, P. Vavpetič, P. Pelicon, P. Kukura, J. L. P. Benesch, K. Iwasaki, and J. G. Heddle, An ultra-stable gold-coordinated protein cage displaying reversible assembly, *Nature* **569**, 438 (2019).
- [41] H. Ren, S. Zhu, and G. Zheng, Nanoreactor Design Based on Self-Assembling Protein Nanocages, *International Journal of Molecular Sciences* **20**, 592 (2019).
- [42] J. Laniado, K. A. Cannon, J. E. Miller, M. R. Sawaya, D. E. McNamara, and T. O. Yeates, Geometric Lessons and Design Strategies for Nanoscale Protein Cages, *ACS Nano* **15**, 4277 (2021).
- [43] S. A. McConnell, K. A. Cannon, C. Morgan, R. McAllister, B. R. Amer, R. T. Clubb, and T. O. Yeates, Designed Protein Cages as Scaffolds for Building Multienzyme Materials, *ACS Synthetic Biology* **9**, 381 (2020).
- [44] A. McMullen, M. Muñoz Basagoiti, Z. Zeravcic, and J. Brujic, Self-assembly of emulsion droplets through programmable folding, *Nature* **610**, 502 (2022).
- [45] T. Garg, G. Rath, and A. K. Goyal, Colloidal Drug Delivery Systems: Current Status and Future Directions, *Critical Reviews in Therapeutic Drug Carrier Systems* **32**, 89 (2015).
- [46] M. Beija, R. Salvayre, N. L.-d. Viguerie, and J.-D. Marty, Colloidal systems for drug delivery: From design to therapy, *Trends in Biotechnology* **30**, 485 (2012).
- [47] S. J. Ebbens, Active colloids: Progress and challenges towards realising autonomous applications, *Current Opinion in Colloid & Interface Science* **21**, 14 (2016).
- [48] S. A. Mallory, C. Valeriani, and A. Cacciuto, An Active Approach to Colloidal Self-Assembly, *Annual Review of Physical Chemistry* **69**, 59 (2018).
- [49] J. A. Fan, Y. He, K. Bao, C. Wu, J. Bao, N. B. Schade, V. N. Manoharan, G. Shvets, P. Nordlander, D. R. Liu, and F. Capasso, DNA-Enabled Self-Assembly of Plasmonic Nanoclusters, *Nano Letters* **11**, 4859 (2011).
- [50] J.-H. Huh, K. Kim, E. Im, J. Lee, Y. Cho, and S. Lee, Exploiting Colloidal Metamaterials for Achieving Unnatural Optical Refractions, *Advanced Materials* **32**, 2001806 (2020).
- [51] Y. Ke, L. L. Ong, W. M. Shih, and P. Yin, Three-Dimensional Structures Self-Assembled from DNA Bricks, *Science* **338**, 1177 (2012).
- [52] D. J. Kraft, J. Groenewold, and W. K. Kegel, Colloidal molecules with well-controlled bond angles, *Soft Matter* **5**, 3823 (2009).
- [53] S. Sacanna, W. T. M. Irvine, P. M. Chaikin, and D. J. Pine, Lock and key colloids, *Nature* **464**, 575 (2010).
- [54] S. Sacanna, M. Korpics, K. Rodriguez, L. Colón-Meléndez, S.-H. Kim, D. J. Pine, and G.-R. Yi, Shaping colloids for self-assembly, *Nature Communications* **4**, 1688 (2013).
- [55] G. R. Yi, D. J. Pine, and S. Sacanna, Recent progress on patchy colloids and their self-assembly, *Journal of Physics: Condensed Matter* **25** (2013).
- [56] J. C.-Y. Wang, D. G. Nickens, T. B. Lentz, D. D. Loeb, and A. Zlotnick, Encapsidated hepatitis B virus reverse transcriptase is poised on an ordered RNA lattice., *Proceedings of the National Academy of Sciences of the United States of America* **111**, 11329 (2014).
- [57] M. He, J. P. Gales, É. Ducrot, Z. Gong, G.-R. Yi, S. Sacanna, and D. J. Pine, Colloidal diamond, *Nature* **585**, 524 (2020).
- [58] M. He, J. P. Gales, X. Shen, M. J. Kim, and D. J. Pine, Colloidal Particles with Triangular Patches, *Langmuir* **37**, 7246 (2021).
- [59] Q. Chen, S. C. Bae, and S. Granick, Directed self-assembly of a colloidal kagome lattice, *Nature* **469**, 381 (2011).
- [60] Q. Chen, J. K. Whitmer, S. Jiang, S. C. Bae, E. Luijten, and S. Granick, Supracolloidal Reaction Kinetics of Janus Spheres, *Science* **331**, 199 (2011).
- [61] D. Zerrouki, J. Baudry, D. Pine, P. Chaikin, and J. Bibette, Chiral colloidal clusters, *Nature* **455**, 380 (2008).
- [62] J. Yan, K. Chaudhary, S. Chul Bae, J. A. Lewis, and S. Granick, Colloidal ribbons and rings from Janus magnetic rods, *Nature Communications* **4**, 1516 (2013).
- [63] J. R. Wolters, G. Avvisati, F. Hagemans, T. Vissers, D. J. Kraft, M. Dijkstra, and W. K. Kegel, Self-assembly of “Mickey Mouse” shaped colloids into tube-like structures: Experiments and simulations, *Soft Matter* **11**, 1067 (2015).
- [64] G. Tikhomirov, P. Petersen, and L. Qian, Triangular DNA Origami Tilings, *Journal of the American Chemical Society* **140**, 17361 (2018).
- [65] J. S. Oh, S. Lee, S. C. Glotzer, G.-R. Yi, and D. J. Pine, Colloidal fibers and rings by cooperative assembly, *Nature Communications* **10**, 3936 (2019).
- [66] A. Ben-Ari, L. Ben-Ari, and G. Bisker, Nonequilibrium self-assembly of multiple stored targets in a dimer-based system, *The Journal of Chemical Physics* **155**, 234113 (2021).
- [67] J. S. Kahn and O. Gang, Designer Nanomaterials through Programmable Assembly, *Angewandte Chemie International Edition* **61**, e202105678 (2022).
- [68] W. M. Jacobs and W. B. Rogers, Assembly of Complex Colloidal Systems Using DNA, *Annual Review of*

- Condensed Matter Physics **16**, 443 (2025).
- [69] M. F. Hagan and D. Chandler, Dynamic pathways for viral capsid assembly, *Biophysical Journal* **91**, 42 (2006).
  - [70] A. W. Wilber, J. P. K. Doye, A. A. Louis, E. G. Noya, M. A. Miller, and P. Wong, Reversible self-assembly of patchy particles into monodisperse icosahedral clusters, *Journal of Chemical Physics* **127**, 085106 (2007).
  - [71] S. Whitelam and R. L. Jack, The statistical mechanics of dynamic pathways to self-assembly, *Ann Rev Phys Chem* **66**, 143 (2015).
  - [72] S. Panahandeh, S. Li, L. Marichal, R. Leite Rubim, G. Tresset, and R. Zandi, How a virus circumvents energy barriers to form symmetric shells, *ACS Nano* **14**, 3170 (2020).
  - [73] H. D. Nguyen, V. S. Reddy, and C. L. Brooks, Deciphering the kinetic mechanism of spontaneous self-assembly of icosahedral capsids, *Nano Letters* **7**, 338 (2007).
  - [74] A. Zlotnick, J. M. Johnson, P. W. Wingfield, S. J. Stahl, and D. Endres, A theoretical model successfully identifies features of hepatitis B virus capsid assembly, *Biochemistry* **38**, 14644 (1999).
  - [75] D. Endres and A. Zlotnick, Model-based analysis of assembly kinetics for virus capsids or other spherical polymers, *Biophysical Journal* **83**, 1217 (2002).
  - [76] A. Zlotnick, Are weak protein-protein interactions the general rule in capsid assembly?, *Virology* **315**, 269 (2003).
  - [77] P. Ceres and A. Zlotnick, Weak protein-protein interactions are sufficient to drive assembly of hepatitis B virus capsids, *Biochemistry* **41**, 11525 (2002).
  - [78] R. L. Jack, M. F. Hagan, and D. Chandler, Fluctuation-dissipation ratios in the dynamics of self-assembly, *Physical Review E: Statistical Physics, Plasmas, Fluids, and Related Interdisciplinary Topics* **76**, 021119 (2007).
  - [79] D. Rapaport, The role of reversibility in viral capsid growth: A paradigm for self-assembly, *Physical Review Letters* **101**, 186101 (2008).
  - [80] S. Whitelam, C. Rogers, A. Pasqua, C. Paavola, J. Trent, and P. L. Geissler, The impact of conformational fluctuations on self-assembly: Cooperative aggregation of archaeal chaperonin proteins, *Nano Letters* **9**, 292 (JAN 2009, 2009).
  - [81] A. W. Wilber, J. P. K. Doye, A. A. Louis, and A. C. F. Lewis, Monodisperse self-assembly in a model with protein-like interactions, *Journal of Chemical Physics* **131**, 175102 (2009).
  - [82] M. F. Hagan, O. M. Elrad, and R. L. Jack, Mechanisms of kinetic trapping in self-assembly and phase transformation, *Journal of Chemical Physics* **135**, 104115 (2011).
  - [83] S. Cheng, A. Aggarwal, and M. J. Stevens, Self-assembly of artificial microtubules, *Soft Matter* **8**, 5666 (2012).
  - [84] M. F. Hagan, Modeling viral capsid assembly, *Special Volume in Memory of Ilya Prigogine* **155**, 1 (2014).
  - [85] J. D. Perlmutter, F. Mohajerani, and M. F. Hagan, Many-molecule encapsulation by an icosahedral shell, *eLife* **5**, e14078 (2016).
  - [86] R. Asor, C. J. Schlicksup, Z. Zhao, A. Zlotnick, and U. Raviv, Rapidly forming early intermediate structures dictate the pathway of capsid assembly, *Journal of the American Chemical Society* **142**, 7868 (2020).
  - [87] Y. Qian, D. Evans, B. Mishra, Y. Fu, Z. H. Liu, S. Guo, and M. E. Johnson, Temporal control by cofactors prevents kinetic trapping in retroviral Gag lattice assembly, *Biophysical Journal* **122**, 3173 (2023).
  - [88] F. Jülicher and C. A. Weber, Droplet Physics and Intracellular Phase Separation, *Annual Review of Condensed Matter Physics* **15**, 237 (2024).
  - [89] A. A. Hyman and K. Simons, Beyond Oil and Water—Phase Transitions in Cells, *Science* **337**, 1047 (2012).
  - [90] J. Berry, C. P. Brangwynne, and M. Haataja, Physical principles of intracellular organization via active and passive phase transitions, *Reports on Progress in Physics* **81**, 046601 (2018).
  - [91] J.-M. Choi, A. S. Holehouse, and R. V. Pappu, Physical Principles Underlying the Complex Biology of Intracellular Phase Transitions, *Annual Review of Biophysics* **49**, 107 (2020).
  - [92] S. F. Banani, H. O. Lee, A. A. Hyman, and M. K. Rosen, Biomolecular condensates: Organizers of cellular biochemistry, *Nature Reviews Molecular Cell Biology* **18**, 285 (2017).
  - [93] W.-K. Cho, J.-H. Spille, M. Hecht, C. Lee, C. Li, V. Grube, and I. I. Cisse, Mediator and RNA polymerase II clusters associate in transcription-dependent condensates, *Science* **361**, 412 (2018).
  - [94] J. E. Henninger, O. Oksuz, K. Shrinivas, I. Sagi, G. LeRoy, M. M. Zheng, J. O. Andrews, A. V. Zamudio, C. Lazaris, N. M. Hannett, T. I. Lee, P. A. Sharp, I. I. Cissé, A. K. Chakraborty, and R. A. Young, RNA-Mediated Feedback Control of Transcriptional Condensates, *Cell* **184**, 207 (2021).
  - [95] D. Hnisz, K. Shrinivas, R. A. Young, A. K. Chakraborty, and P. A. Sharp, A Phase Separation Model for Transcriptional Control, *Cell* **169**, 13 (2017).
  - [96] B. R. Sabari, A. Dall'Agnese, A. Boija, I. A. Klein, E. L. Coffey, K. Shrinivas, B. J. Abraham, N. M. Hannett, A. V. Zamudio, J. C. Manteiga, C. H. Li, Y. E. Guo, D. S. Day, J. Schuijers, E. Vasile, S. Malik, D. Hnisz, T. I. Lee, I. I. Cisse, R. G. Roeder, P. A. Sharp, A. K. Chakraborty, and R. A. Young, Coactivator condensation at super-enhancers links phase separation and gene control, *Science* **361**, eaar3958 (2018).
  - [97] S. Chong, C. Dugast-Darzacq, Z. Liu, P. Dong, G. M. Dailey, C. Cattoglio, A. Heckert, S. Banala, L. Lavis, X. Darzacq, and R. Tjian, Imaging dynamic and selective low-complexity domain interactions that control gene transcription, *Science* **361**, eaar2555 (2018).
  - [98] R. Parker and U. Sheth, P Bodies and the Control of mRNA Translation and Degradation, *Molecular Cell* **25**, 635 (2007).
  - [99] C. P. Brangwynne, C. R. Eckmann, D. S. Courson, A. Rybarska, C. Hoege, J. Gharakhani, F. Jülicher, and A. A. Hyman, Germline P Granules Are Liquid Droplets That Localize by Controlled Dissolution/Condensation, *Science* **324**, 1729 (2009).
  - [100] X. Wu, Q. Cai, Z. Feng, and M. Zhang, Liquid-Liquid Phase Separation in Neuronal Development and Synaptic Signaling, *Developmental Cell* **55**, 18 (2020).
  - [101] T. B. Stanishneva-Konovalova, C. F. Kelley, T. L. Eskin, E. M. Messelaar, S. A. Wasserman, O. S. Sokolova, and A. A. Rodal, Coordinated autoinhibition of F-BAR domain membrane binding and WASp activation by Nervous Wreck, *Proceedings of the National Academy of Sciences* **113**, E5552 (2016).
  - [102] S. J. Del Signore, C. F. Kelley, E. M. Messelaar, T. Lemos, M. F. Marchan, B. Ermanoska, M. Mund,

- T. G. Fai, M. Kaksonen, and A. A. Rodal, An autoinhibitory clamp of actin assembly constrains and directs synaptic endocytosis, *eLife* **10**, e69597 (2021).
- [103] K. J. Day, G. Kago, L. Wang, J. B. Richter, C. C. Hayden, E. M. Lafer, and J. C. Stachowiak, Liquid-like protein interactions catalyse assembly of endocytic vesicles, *Nature cell biology* **23**, 366 (2021).
- [104] M. Zeng, X. Chen, D. Guan, J. Xu, H. Wu, P. Tong, and M. Zhang, Reconstituted postsynaptic density as a molecular platform for understanding synapse formation and plasticity, *Cell* **174**, 1172 (2018).
- [105] N. A. McDonald, R. D. Fetter, and K. Shen, Assembly of synaptic active zones requires phase separation of scaffold molecules, *Nature* **588**, 454 (2020).
- [106] J. Emperador-Melero, M. Y. Wong, S. S. H. Wang, G. de Nola, H. Nyitrai, T. Kirchhausen, and P. S. Kaeser, PKC-phosphorylation of Liprin- $\alpha$ 3 triggers phase separation and controls presynaptic active zone structure, *Nature Communications* **12**, 3057 (2021).
- [107] W. P. Lipiński, B. S. Visser, I. Robu, M. A. A. Fakhree, S. Lindhoud, M. M. A. E. Claessens, and E. Spruijt, Biomolecular condensates can both accelerate and suppress aggregation of  $\alpha$ -synuclein, *bioRxiv : the preprint server for biology*, 2022.04.22.489149 (2022).
- [108] P. M. McCall, S. Srivastava, S. L. Perry, D. R. Kovar, M. L. Gardel, and M. V. Tirrell, Partitioning and Enhanced Self-Assembly of Actin in Polypeptide Coacervates, *Biophysical Journal* **114**, 1636 (2018).
- [109] A. Borodavka, U. Desselberger, and J. T. Patton, Genome packaging in multi-segmented dsRNA viruses: Distinct mechanisms with similar outcomes, *Current opinion in virology* **33**, 106 (2018).
- [110] A. Borodavka, E. C. Dykeman, W. Schrimpf, and D. C. Lamb, Protein-mediated RNA folding governs sequence-specific interactions between rotavirus genome segments, *eLife* **6**, e27453 (2017).
- [111] S. Brocca, R. Grandori, S. Longhi, and V. Uversky, Liquid-liquid phase separation by intrinsically disordered protein regions of viruses: Roles in viral life cycle and control of virus-host interactions, *International journal of molecular sciences* **21**, 10.3390/ijms21239045 (2020).
- [112] C. R. Carlson, J. B. Asfaha, C. M. Ghent, C. J. Howard, N. Hartooni, and D. O. Morgan, Phosphorylation modulates liquid-liquid phase separation of the SARS-CoV-2 N protein, *bioRxiv : the preprint server for biology* 10.1101/2020.06.28.176248 (2020).
- [113] T. A. Etibor, Y. Yamauchi, and M. J. Amorim, Liquid biomolecular condensates and viral lifecycles: Review and perspectives, *Viruses* **13**, 10.3390/v13030366 (2021).
- [114] I. Fernández de Castro, R. Tenorio, and C. Risco, Virus factories, in *Reference Module in Life Sciences* (2020).
- [115] A. Gaete-Argel, C. L. Márquez, G. P. Barriga, R. Soto-Rifo, and F. Valiente-Echeverría, Strategies for Success. Viral Infections and Membraneless Organelles, *Frontiers in Cellular and Infection Microbiology* **9**, 10.3389/fcimb.2019.00336 (2019).
- [116] F. Geiger, J. Acker, G. Papa, X. Wang, W. E. Arter, K. L. Saar, N. A. Erkamp, R. Qi, J. P. Bravo, S. Strauss, G. Krainer, O. R. Burrone, R. Jungmann, T. P. Knowles, H. Engelke, and A. Borodavka, Liquid-liquid phase separation underpins the formation of replication factories in rotaviruses, *The EMBO Journal* **40**, e107711 (2021).
- [117] S. Guseva, S. Milles, M. R. Jensen, N. Salvi, J.-P. Kleman, D. Maurin, R. W. H. Ruigrok, and M. Blackledge, Measles virus nucleo- and phosphoproteins form liquid-like phase-separated compartments that promote nucleocapsid assembly, *Science Advances* **6**, eaaz7095 (2020).
- [118] Q. Kieser, R. S. Noyce, M. Shenouda, Y. J. Lin, and D. H. Evans, Cytoplasmic factories, virus assembly, and DNA replication kinetics collectively constrain the formation of poxvirus recombinants, *PLoS One* **15**, e0228028 (2020).
- [119] N. Lopez, G. Camporeale, M. Salgueiro, S. S. Borkosky, A. Visentin, R. Peralta-Martinez, M. E. Loureiro, and G. de Prat-Gay, Deconstructing virus condensation, *PLoS pathogens* **17**, e1009926 (2021).
- [120] D. Luque and J. R. Caston, Cryo-electron microscopy for the study of virus assembly, *Nature chemical biology* **16**, 231 (2020).
- [121] J. Nikolic, R. Le Bars, Z. Lama, N. Scrima, C. Lagaudriere-Gesbert, Y. Gaudin, and D. Blondel, Negri bodies are viral factories with properties of liquid organelles, *Nature communications* **8**, 58 (2017).
- [122] M. Pan, A. L. Alvarez-Cabrera, J. S. Kang, L. Wang, C. Fan, and Z. H. Zhou, Asymmetric reconstruction of mammalian reovirus reveals interactions among RNA, transcriptional factor micro2 and capsid proteins, *Nature communications* **12**, 4176 (2021).
- [123] G. Papa, A. Borodavka, and U. Desselberger, Viroplasm: Assembly and functions of rotavirus replication factories, *Viruses* **13**, 10.3390/v13071349 (2021).
- [124] J. Risso-Ballester, M. Galloux, J. Cao, R. Le Goffic, F. Hontonnou, A. Jobart-Malfait, A. Desquesnes, S. M. Sake, S. Haid, M. Du, X. Zhang, H. Zhang, Z. Wang, V. Rincheval, Y. Zhang, T. Pietschmann, J. F. Eleouet, M. A. Rameix-Welti, and R. Altmeyer, A condensate-hardening drug blocks RSV replication in vivo, *Nature* **595**, 596 (2021).
- [125] A. Savastano, A. Ibanez de Opakua, M. Rankovic, and M. Zweckstetter, Nucleocapsid protein of SARS-CoV-2 phase separates into RNA-rich polymerase-containing condensates, *Nature communications* **11**, 6041 (2020).
- [126] J. E. Schoelz and S. Leisner, Setting up shop: The formation and function of the viral factories of cauliflower mosaic virus, *Frontiers in plant science* **8**, 1832 (2017).
- [127] S. D. Trask, S. M. McDonald, and J. T. Patton, Structural insights into the coupling of virion assembly and rotavirus replication, *Nature reviews. Microbiology* **10**, 165 (2012).
- [128] S. Wang, T. Dai, Z. Qin, T. Pan, F. Chu, L. Lou, L. Zhang, B. Yang, H. Huang, H. Lu, and F. Zhou, Targeting liquid-liquid phase separation of SARS-CoV-2 nucleocapsid protein promotes innate antiviral immunity by elevating MAVS activity, *Nature Cell Biology* **23**, 718 (2021).
- [129] G. Papa, L. Venditti, F. Arnoldi, E. M. Schraner, C. Potgieter, A. Borodavka, C. Eichwald, and O. R. Burrone, Recombinant Rotaviruses Rescued by Reverse Genetics Reveal the Role of NSP5 Hyperphosphorylation in the Assembly of Viral Factories, *Journal of Virology* **94**, e01110 (2019).
- [130] D. Zwicker, M. Decker, S. Jaensch, A. A. Hyman, and F. Jülicher, Centrosomes are autocatalytic droplets of pericentriolar material organized by centrioles, *Proceedings of the National Academy of Sciences* **111**, E2636

- (2014).
- [131] D. Zwicker, A. A. Hyman, and F. Jülicher, Suppression of Ostwald ripening in active emulsions, *Physical Review E* **92**, 012317 (2015).
  - [132] D. Zwicker, R. Seyboldt, C. A. Weber, A. A. Hyman, and F. Jülicher, Growth and division of active droplets provides a model for protocells, *Nature Physics* **13**, 408 (2017).
  - [133] D. Zwicker, O. W. Paulin, and C. ter Burg, Physics of droplet regulation in biological cells (2025).
  - [134] C. A. Weber, D. Zwicker, F. Jülicher, and C. F. Lee, Physics of active emulsions, *Reports on Progress in Physics* **82**, 064601 (2019).
  - [135] N. Ziethen, J. Kirschbaum, and D. Zwicker, Nucleation of Chemically Active Droplets, *Physical Review Letters* **130**, 248201 (2023).
  - [136] N. Ziethen and D. Zwicker, Heterogeneous nucleation and growth of sessile chemically active droplets, *The Journal of Chemical Physics* **160**, 224901 (2024).
  - [137] J. Söding, D. Zwicker, S. Sohrabi-Jahromi, M. Boehning, and J. Kirschbaum, Mechanisms for Active Regulation of Biomolecular Condensates, *Trends in Cell Biology* **30**, 4 (2020).
  - [138] J. Kirschbaum and D. Zwicker, Controlling biomolecular condensates via chemical reactions, *Journal of The Royal Society Interface* **18**, 20210255 (2021).
  - [139] C. Luo, N. Hess, D. Aierken, Y. Qiang, J. A. Joseph, and D. Zwicker, Condensate Size Control by Net Charge (2025).
  - [140] R. Rossetto, G. Wellecke, and D. Zwicker, Binding and dimerization control phase separation in a compartment (2024).
  - [141] J.-M. Choi, F. Dar, and R. V. Pappu, LASSI: A lattice model for simulating phase transitions of multivalent proteins, *PLOS Computational Biology* **15**, e1007028 (2019).
  - [142] C. P. Brangwynne, P. Tompa, and R. V. Pappu, Polymer physics of intracellular phase transitions, *Nature Physics* **11**, 899 (2015).
  - [143] K. M. Ruff, R. V. Pappu, and A. S. Holehouse, Conformational preferences and phase behavior of intrinsically disordered low complexity sequences: Insights from multiscale simulations, *Current Opinion in Structural Biology Sequences and Topology* **56**, 1 (2019).
  - [144] A. Holla, E. W. Martin, T. Dannenhoffer-Lafage, K. M. Ruff, S. L. B. König, M. F. Nüesch, A. Chowdhury, J. M. Louis, A. Soranno, D. Nettels, R. V. Pappu, R. B. Best, T. Mittag, and B. Schuler, Identifying Sequence Effects on Chain Dimensions of Disordered Proteins by Integrating Experiments and Simulations, *JACS Au* **4**, 4729 (2024).
  - [145] G. L. Dignon, W. Zheng, R. B. Best, Y. C. Kim, and J. Mittal, Relation between single-molecule properties and phase behavior of intrinsically disordered proteins, *Proceedings of the National Academy of Sciences* **115**, 9929 (2018).
  - [146] G. L. Dignon, W. Zheng, and J. Mittal, Simulation methods for liquid–liquid phase separation of disordered proteins, *Current Opinion in Chemical Engineering Frontiers of Chemical Engineering: Molecular Modeling*, **23**, 92 (2019).
  - [147] G. L. Dignon, W. Zheng, Y. C. Kim, and J. Mittal, Temperature-Controlled Liquid–Liquid Phase Separation of Disordered Proteins, *ACS Central Science* **5**, 821 (2019).
  - [148] J.-E. Shea, R. B. Best, and J. Mittal, Physics-based computational and theoretical approaches to intrinsically disordered proteins, *Current Opinion in Structural Biology Theory and Simulation/Computational Methods* **67**, 219 (2021).
  - [149] S. Rekhi, C. G. Garcia, M. Barai, A. Rizuan, B. S. Schuster, K. L. Kiick, and J. Mittal, Expanding the molecular language of protein liquid–liquid phase separation, *Nature Chemistry* **16**, 1113 (2024).
  - [150] U. Kapoor, Y. C. Kim, and J. Mittal, Coarse-Grained Models to Study Protein–DNA Interactions and Liquid–Liquid Phase Separation, *Journal of Chemical Theory and Computation* **20**, 1717 (2024).
  - [151] H. H. Schede, P. Natarajan, A. K. Chakraborty, and K. Shrinivas, A model for organization and regulation of nuclear condensates by gene activity, *Nature Communications* **14**, 4152 (2023).
  - [152] S. F. Banani, A. Goychuk, P. Natarajan, M. M. Zheng, G. Dall’Agnese, J. E. Henninger, M. Kardar, R. A. Young, and A. K. Chakraborty, Active RNA synthesis patterns nuclear condensates, *bioRxiv*, 2024.10.12.614958 (2024).
  - [153] A. G. T. Pyo, Y. Zhang, and N. S. Wingreen, Proximity to criticality predicts surface properties of biomolecular condensates, *Proceedings of the National Academy of Sciences* **120**, e2220014120 (2023).
  - [154] T. GrandPre, Y. Zhang, A. G. T. Pyo, B. Weiner, J.-L. Li, M. C. Jonikas, and N. S. Wingreen, Impact of Linker Length on Biomolecular Condensate Formation, *PRX Life* **1**, 023013 (2023).
  - [155] Y. Zhang, A. G. Pyo, R. Kliegman, Y. Jiang, C. P. Brangwynne, H. A. Stone, and N. S. Wingreen, The exchange dynamics of biomolecular condensates, *eLife* **12**, RP91680 (2024).
  - [156] V. Grigorev, N. S. Wingreen, and Y. Zhang, Conformational Entropy of Intrinsically Disordered Proteins Bars Intruders from Biomolecular Condensates, *PRX Life* **3**, 013011 (2025).
  - [157] W. M. Jacobs, Self-assembly of biomolecular condensates with shared components, *Physical review letters* **126**, 258101 (2021).
  - [158] F. Chen and W. M. Jacobs, Emergence of Multiphase Condensates from a Limited Set of Chemical Building Blocks, *Journal of Chemical Theory and Computation* **20**, 6881 (2024).
  - [159] T. Li and W. M. Jacobs, Predicting the Morphology of Multiphase Biomolecular Condensates from Protein Interaction Networks, *PRX Life* **2**, 023013 (2024).
  - [160] Y.-H. Lin, J. D. Forman-Kay, and H. S. Chan, Theories for Sequence-Dependent Phase Behaviors of Biomolecular Condensates, *Biochemistry* **57**, 2499 (2018).
  - [161] H. Cinar, Z. Fetahaj, S. Cinar, R. M. Vernon, H. S. Chan, and R. H. A. Winter, Temperature, Hydrostatic Pressure, and Osmolyte Effects on Liquid–Liquid Phase Separation in Protein Condensates: Physical Chemistry and Biological Implications, *Chemistry – A European Journal* **25**, 13049 (2019).
  - [162] T. Pal, J. Wessén, S. Das, and H. S. Chan, Subcompartmentalization of polyampholyte species in organelle-like condensates is promoted by charge-pattern mismatch and strong excluded-volume interaction, *Physical Review E* **103**, 042406 (2021).

- [163] Z. Shen, B. Jia, Y. Xu, J. Wessén, T. Pal, H. S. Chan, S. Du, and M. Zhang, Biological condensates form percolated networks with molecular motion properties distinctly different from dilute solutions, *eLife* **12**, e81907 (2023).
- [164] S. Das, A. N. Amin, Y.-H. Lin, and H. Sun Chan, Coarse-grained residue-based models of disordered protein condensates: Utility and limitations of simple charge pattern parameters, *Physical Chemistry Chemical Physics* **20**, 28558 (2018).
- [165] V. Nguemaha and H.-X. Zhou, Liquid-Liquid Phase Separation of Patchy Particles Illuminates Diverse Effects of Regulatory Components on Protein Droplet Formation, *Scientific Reports* **8**, 6728 (2018).
- [166] D. Kota and H.-X. Zhou, Macromolecular Regulation of the Material Properties of Biomolecular Condensates, *The Journal of Physical Chemistry Letters* **13**, 5285 (2022).
- [167] H.-X. Zhou, D. Kota, S. Qin, and R. Prasad, Fundamental Aspects of Phase-Separated Biomolecular Condensates, *Chemical Reviews* **124**, 8550 (2024).
- [168] G. Bartolucci, I. S. Haugerud, T. C. T. Michaels, and C. A. Weber, The interplay between biomolecular assembly and phase separation, *eLife* **13**, 10.7554/eLife.93003.1 (2024).
- [169] M. F. Hagan and F. Mohajerani, Self-assembly coupled to liquid-liquid phase separation, *PLOS Computational Biology* **19**, e1010652 (2023).
- [170] J. A. Ditlev, L. B. Case, and M. K. Rosen, Who's In and Who's Out-Compositional Control of Biomolecular Condensates, *Journal of Molecular Biology* **430**, 4666 (2018).
- [171] F. Mohajerani, B. Tyukodi, C. J. Schlicksup, J. A. Hadden-Perilla, A. Zlotnick, and M. F. Hagan, Multi-scale Modeling of Hepatitis B Virus Capsid Assembly and Its Dimorphism, *ACS Nano* **16**, 13845 (2022).
- [172] M. F. Hagan and G. M. Grason, Equilibrium mechanisms of self-limiting assembly, *Reviews of Modern Physics* **93**, 025008 (2021).
- [173] S. Li, P. Roy, A. Travesset, and R. Zandi, Why large icosahedral viruses need scaffolding proteins, *Proceedings of the National Academy of Sciences of the United States of America* **115**, 10971 (2018).
- [174] R. Schwartz, R. L. Garcea, and B. Berger, "Local rules" theory applied to polyomavirus polymorphic capsid assemblies, *Virology* **268**, 461 (2000).
- [175] D. Rapaport, Self-assembly of polyhedral shells: A molecular dynamics study, *Physical Review E* **70**, 051905 (2004).
- [176] H. D. Nguyen, V. S. Reddy, and C. L. Brooks, Invariant polymorphism in virus capsid assembly, *Journal of The American Chemical Society* **131**, 2606 (2009).
- [177] O. M. Elrad and M. F. Hagan, Mechanisms of size control and polymorphism in viral capsid assembly, *Nano Letters* **8**, 3850 (2008).
- [178] I. G. Johnston, A. A. Louis, and J. P. K. Doye, Modelling the self-assembly of virus capsids, *Journal of Physics: Condensed Matter* **22**, 104101 (2010).
- [179] D. C. Rapaport, Studies of reversible capsid shell growth, *Journal of Physics: Condensed Matter* **22**, 104115 (2010).
- [180] HD. Nguyen and CL. Brooks, Generalized structural polymorphism in self-assembled viral particles, *Nano Letters* **8**, 4574 (2008).
- [181] R. Schwartz, P. W. Shor, P. E. Prevelige, and B. Berger, Local rules simulation of the kinetics of virus capsid self-assembly, *Biophysical Journal* **75**, 2626 (1998).
- [182] B. Sweeney, T. Zhang, and R. Schwartz, Exploring the parameter space of complex self-assembly through virus capsid models, *Biophysical Journal* **94**, 772 (2008).
- [183] B. Tyukodi, F. Mohajerani, D. M. Hall, G. M. Grason, and M. F. Hagan, Thermodynamic size control in curvature-frustrated tubules: Self-limitation with open boundaries, *ACS Nano* 10.1021/acsnano.2c00865 (2022).
- [184] H. Fang, B. Tyukodi, W. B. Rogers, and M. F. Hagan, Polymorphic self-assembly of helical tubules is kinetically controlled, *Soft Matter* **18**, 6716 (2022).
- [185] G. M. Rotskoff and P. L. Geissler, Robust nonequilibrium pathways to microcompartment assembly, *Proceedings of the National Academy of Sciences of the United States of America* **115**, 6341 (2018).
- [186] J. A. Anderson, J. Glaser, and S. C. Glotzer, HOOMD-blue: A Python package for high-performance molecular dynamics and hard particle Monte Carlo simulations, *Computational Materials Science* **173**, 109363 (2020).
- [187] J. D. Perlmutter, C. Qiao, and M. F. Hagan, Viral genome structures are optimal for capsid assembly, *eLife* **2**, e00632 (2013).
- [188] J. D. Perlmutter, M. R. Perkett, and M. F. Hagan, Pathways for virus assembly around nucleic acids, *Journal of Molecular Biology* 10.1016/j.jmb.2014.07.004 (2014).
- [189] J. D. Weeks, D. Chandler, and H. C. Andersen, Role of Repulsive Forces in Determining the Equilibrium Structure of Simple Liquids, *The Journal of Chemical Physics* **54**, 5237 (1971).
- [190] N. F. Carnahan and K. E. Starling, Equation of State for Nonattracting Rigid Spheres, *The Journal of Chemical Physics* **51**, 635 (1969).
- [191] N. F. Carnahan and K. E. Starling, Thermodynamic Properties of a Rigid-Sphere Fluid, *The Journal of Chemical Physics* **53**, 600 (1970).
- [192] G. A. Mansoori, N. F. Carnahan, K. E. Starling, and T. W. Leland, Equilibrium Thermodynamic Properties of the Mixture of Hard Spheres, *The Journal of Chemical Physics* **54**, 1523 (1971).
- [193] A. Trubiano, Self-Assembly Analysis Suite for HOOMD, <https://github.com/onehalfatsquared/SAASH> (2024).
- [194] S. Katen and A. Zlotnick, Chapter 14 The Thermodynamics of Virus Capsid Assembly, in *Methods in Enzymology*, Biothermodynamics, Part A, Vol. 455 (Academic Press, 2009) pp. 395–417.
- [195] R. F. Bruinsma, G. J. L. Wuite, and W. H. Roos, Physics of viral dynamics, *Nature Reviews Physics* **3**, 76 (2021).
- [196] M. F. Hagan and O. Elrad, Understanding the concentration dependence of viral capsid assembly kinetics - the origin of the lag time and identifying the critical nucleus size, *Biophysical Journal* **98**, 1065 (2010).
- [197] A. Zlotnick, R. Aldrich, J. M. Johnson, P. Ceres, and M. J. Young, Mechanism of capsid assembly for an icosahedral plant virus, *Virology* **277**, 450 (2000).
- [198] P. K. Sorger, P. G. Stockley, and S. C. Harrison, Structure and assembly of turnip crinkle virus. 2. Mechanism of reassembly in vitro, *Journal of Molecular Biology* **191**, 639 (1986).
- [199] K. N. Parent, M. M. Suhanovsky, and C. M. Teschke, Polyhead formation in phage P22 pinpoints a region



- in coat protein required for conformational switching, *Molecular Microbiology* **65**, 1300 (2007).
- [200] S. J. Stray, C. R. Bourne, S. Punna, W. G. Lewis, M. G. Finn, and A. Zlotnick, A heteroaryldihydropyrimidine activates and can misdirect hepatitis B virus capsid assembly, *Proceedings of the National Academy of Sciences of the United States of America* **102**, 8138 (2005).
- [201] P. Kondylis, C. J. Schlicksup, N. E. Brunk, J. Zhou, A. Zlotnick, and S. C. Jacobson, Competition between normative and drug-induced virus self-assembly observed with single-particle methods, *Journal of the American Chemical Society* **141**, 1251 (2018).
- [202] A. Trubiano and M. F. Hagan, Markov state model approach to simulate self-assembly, (2024).
- [203] M. Castelnovo, T. Verdier, and L. Foret, Comparing open and closed molecular self-assembly, *Epl-europhys Lett* **105**, 10.1209/0295-5075/105/28006 (2014).
- [204] W. Pönisch, T. C. Michaels, and C. A. Weber, Aggregation controlled by condensate rheology, *bioRxiv : the preprint server for biology*, 2021.11.05.467474 (2021).
- [205] J. D. Schmit and T. C. T. Michaels, Physical limits to acceleration of enzymatic reactions inside phase-separated compartments, *Physical Review E* **109**, 064401 (2024).
- [206] L. P. Bergeron-Sandoval, N. Safaei, and S. W. Michnick, Mechanisms and consequences of macromolecular phase separation, *Cell* **165**, 1067 (2016).
- [207] T. E. Videbæk, D. Hayakawa, M. F. Hagan, G. M. Grason, S. Fraden, and W. B. Rogers, Measuring multisubunit mechanics of geometrically-programmed colloidal assemblies via cryo-EM multi-body refinement, (2025).
- [208] R. Asor, O. Ben-nun-Shaul, A. Oppenheim, and U. Raviv, Crystallization, Reentrant Melting, and Resolubilization of Virus Nanoparticles, *ACS Nano* **11**, 9814 (2017).
- [209] M. Uchida, K. McCoy, M. Fukuto, L. Yang, H. Yoshimura, H. M. Miettinen, B. LaFrance, D. P. Patterson, B. Schwarz, J. A. Karty, P. E. J. Prevelige, B. Lee, and T. Douglas, Modular Self-Assembly of Protein Cage Lattices for Multistep Catalysis, *ACS Nano* **12**, 942 (2018).
- [210] K. McCoy, M. Uchida, B. Lee, and T. Douglas, Templated Assembly of a Functional Ordered Protein Macromolecular Framework from P22 Virus-like Particles, *ACS Nano* **12**, 3541 (2018).
- [211] B. K. Ganser-Pornillos, U. K. von Schwedler, K. M. Stray, C. Aiken, and W. I. Sundquist, Assembly properties of the human immunodeficiency virus-1 CA protein, *J. Virol* **78**, 2545 (2004).
- [212] B. K. Ganser-Pornillos, M. Yeager, and W. I. Sundquist, The structural biology of HIV assembly, *Current Opinion in Structural Biology* **18**, 203 (2008).
- [213] Z. Yu, M. J. Dobro, A. Levandovsky, C. M. Danielson, V. Sandrin, J. Shi, C. Aiken, R. Zandi, T. J. Hope, and G. J. Jensen, Unclosed HIV-1 capsids suggest a curled sheet model of assembly, *JMB* **425**, 112 (2013).
- [214] M. V. Nermut, W. H. Zhang, G. Francis, F. Ciampor, Y. Morikawa, and I. M. Jones, Time course of gag protein assembly in HIV-1-infected cells: A study by immunoelectron microscopy, *Virology* **305**, 219 (2003).
- [215] C. S. Adamson and I. M. Jones, The molecular basis of HIV capsid assembly - five years of progress, *Reviews in Medical Virology* **14**, 107 (2004).
- [216] J. A. Briggs, K. Grünewald, B. Glass, F. Förster, H.-G. Kräusslich, and S. D. Fuller, The mechanism of HIV-1 core assembly: Insights from three-dimensional reconstructions of authentic virions, *Structure (London, England : 1993)* **14**, 15 (2006).
- [217] B. Chen and R. Tycko, Simulated self-assembly of the HIV-1 capsid: Protein shape and native contacts are sufficient for two-dimensional lattice formation, *Biophysical Journal* **100**, 3035 (2011).
- [218] V. Krishna, G. S. Ayton, and G. A. Voth, Role of protein interactions in defining HIV-1 viral capsid shape and stability: A coarse-grained analysis, *Biophysical Journal* **98**, 18 (2010).
- [219] V. Baumgaertel, B. Mueller, and D. C. Lamb, Quantitative live-cell imaging of human immunodeficiency virus (HIV-1) assembly, *Viruses* **4**, 777 (2012).
- [220] M. Balasubramaniam and E. O. Freed, New insights into HIV assembly and trafficking, *Physiology* **26**, 236 (2011).
- [221] G. Zhao, J. R. Perilla, E. L. Yufenyuy, X. Meng, B. Chen, J. Ning, J. Ahn, A. M. Gronenborn, K. Schulten, C. Aiken, and P. Zhang, Mature HIV-1 capsid structure by cryo-electron microscopy and all-atom molecular dynamics., *Nature* **497**, 643 (2013).
- [222] J. M. A. Grime and G. A. Voth, Early stages of the HIV-1 capsid protein lattice formation, *Biophysical Journal* **103**, 1774 (2012).
- [223] M. Gupta, A. J. Pak, and G. A. Voth, Critical mechanistic features of HIV-1 viral capsid assembly, *Science advances* **9**, eadd7434 (2023).